

**AD-A279 342**



**RL-TR-93-259**  
**In-House Report**  
**December 1993**



**HETEROSTRUCTURE QUANTUM  
CONFINED STARK EFFECT ELECTRO-  
OPTIC MODULATORS OPERATING AT 938  
nm**

**Michael J. Hayduk, Mark F. Krol, Raymond K. Boncek**

**DTIC**  
**ELECTE**  
**MAY 18 1994**  
**S G D**

*APPROVED FOR PUBLIC RELEASE; DISTRIBUTION UNLIMITED.*

**94-14863**



**Rome Laboratory**  
**Air Force Materiel Command**  
**Griffiss Air Force Base, New York**

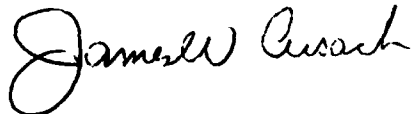
**DTIC QUALITY INSPECTED 1**

**94 5 17 164**

This report has been reviewed by the Rome Laboratory Public Affairs Office (PA) and is releasable to the National Technical Information Service (NTIS). At NTIS it will be releasable to the general public, including foreign nations.

RL-TR-93-259 has been reviewed and is approved for publication.

APPROVED:



JAMES W. CUSACK, Chief  
Photonics & Optics Division  
Surveillance & Photonics Directorate

FOR THE COMMANDER:



DONALD W. HANSON  
Director of Surveillance & Photonics

If your address has changed or if you wish to be removed from the Rome Laboratory mailing list, or if the addressee is no longer employed by your organization, please notify RL ( OCPA ) Griffiss AFB NY 13441. This will assist us in maintaining a current mailing list.

Do not return copies of this report unless contractual obligations or notices on a specific document require that it be returned.

REPORT DOCUMENTATION PAGE			Form Approved OMB No. 0704-0188	
Public reporting burden for this collection of information is estimated to average 1 hour per response, including the time for reviewing instructions, searching existing data sources, gathering and maintaining the data needed, and completing and reviewing the collection of information. Send comments regarding this burden estimate or any other aspect of this collection of information, including suggestions for reducing this burden, to Washington Headquarters Services, Directorate for Information Operations and Reports, 1215 Jefferson Davis Highway, Suite 1204, Arlington, VA 22202-4302, and to the Office of Management and Budget, Paperwork Reduction Project (0704-0188), Washington, DC 20503.				
1. AGENCY USE ONLY (Leave Blank)		2. REPORT DATE December 1993		3. REPORT TYPE AND DATES COVERED In-House May 92 - May 93
4. TITLE AND SUBTITLE HETEROSTRUCTURE QUANTUM CONFINED STARK EFFECT ELECTRO- OPTIC MODULATORS OPERATING AT 938 nm			5. FUNDING NUMBERS PE - 62702F PR - 4600 TA - P2 WL - 06	
6. AUTHOR(S) Michael J. Hayduk, Mark F. Krol, Raymond K. Boncek				
7. PERFORMING ORGANIZATION NAME(S) AND ADDRESS(ES) Rome Laboratory (OCPA) 25 Electronic Pky Griffiss AFB NY 13441-4515			8. PERFORMING ORGANIZATION REPORT NUMBER RL-TR-93-259	
9. SPONSORING/MONITORING AGENCY NAME(S) AND ADDRESS(ES) Rome Laboratory (OCPA) 25 Electronic Pky Griffiss AFB NY 13441-4515			10. SPONSORING/MONITORING AGENCY REPORT NUMBER	
11. SUPPLEMENTARY NOTES Rome Laboratory Project Engineer: Michael J. Hayduk/OCPA (315) 330-4456				
12a. DISTRIBUTION/AVAILABILITY STATEMENT Approved for public release; distribution unlimited.			12b. DISTRIBUTION CODE	
13. ABSTRACT (Maximum 200 words) Electro-optic modulators are a necessary component of emerging optical fiber based local area interconnects. One type of modulator, suitable for use in optical interconnects, is an asymmetric Fabry-Perot reflection modulator (ARM). This type of an intensity modulator uses an electro-optic material as the spacer material to balance the normally unequal front and back mirror reflectances. The quantum confined Franz-Keldysh and Stark effects shift the absorption edge of semiconductor multiple quantum well (MQW) materials to longer wavelengths in the presence of an external electric field applied perpendicular to the MQW layers, thereby changing the reflectance of the etalon. The combined coherence effects of the etalon coupled with the quantum effects of the MQW materials result in a large modulation depth and a low insertion loss. P-I-N diode structures using an In Ga As/GaAs MQW structure as the intrinsic region were fabricated for the purpose of characterizing the electro-absorption associated with different applied electric fields. Quantum confined Franz-Keldysh and Stark shifts were observed for applied electric fields as large as $6.58 \times 10^4$ V/cm. The resulting change in the absorption coefficient was found to be $-3.7 \times 10^3$ cm <sup>-1</sup> which is sufficient to design a high-speed ARM with a large modulation depth and a low insertion loss.				
14. SUBJECT TERMS electro-optics, Stark effect, modulator, quantum wells, InGaAs/GaAs			15. NUMBER OF PAGES 88	
			16. PRICE CODE	
17. SECURITY CLASSIFICATION OF REPORT UNCLASSIFIED	18. SECURITY CLASSIFICATION OF THIS PAGE UNCLASSIFIED	19. SECURITY CLASSIFICATION OF ABSTRACT UNCLASSIFIED	20. LIMITATION OF ABSTRACT U/L	

## Table of Contents

List of figures.....	ii
List of tables.....	iv
List of symbols.....	v
Chapter 1 Introduction.....	1
Chapter 2 Asymmetric Fabry-Perot Theory.....	7
2.1 Single layer theory.....	7
2.2 Multiple layer theory.....	15
2.3 Design, growth and characterization of GaAs/AlAs DBR.....	20
Chapter 3 Optical and Electro-optical Properties of Quantum Well Structures.....	24
3.1 Quantum well theory.....	24
3.2 Optical absorption properties of quantum wells.....	31
3.3 Electro-optical properties of quantum wells.....	39
Chapter 4 Electro-absorption Characterization of InGaAs/GaAs Multiple Quantum Wells.....	49
4.1 Growth and processing of InGaAs/GaAs quantum wells.....	49
4.2 Electro-absorption experimental setup and results.....	54
Chapter 5 Conclusions and Recommendations for Work.....	63
5.1 Design of asymmetric reflection modulator.....	63
5.2 Conclusions and recommendations for future work.....	65
Appendix A Fabrication and Processing Techniques for P-I-N structures.....	67
References.....	72

## List of Figures

Figure	Page
1-1 Schematic diagram of asymmetric reflection modulator	3
2-1a Single layer asymmetric Fabry-Perot etalon	9
2-1b Round trip phase shift in Fabry-Perot etalon	9
2-2 Reflectance at resonance versus spacer absorbance for a single layer etalon	14
2-3 Calculated reflectance spectra for 10 and 15 period DBRs	19
2-4 Measured 15 period reflectance spectrum of 15 period GaAs/AlAs DBR	22
3-1 Schematic band structure for a single quantum well	25
3-2 The dispersion relation, Energy versus $k_{x,y}$ , in momentum space for a single quantum well	29
3-3 Well width dependence of the first allowed transition of a single quantum well	32
3-4 Optical free carrier absorption spectrum of a single quantum well	34
3-5 Schematic comparison of the 2-d free carrier (dashed line) and excitonic (solid line) optical absorption spectra	37
3-6 Optical absorption spectrum of an $\text{In}_{0.2}\text{Ga}_{0.8}\text{As}/\text{GaAs}$ MQW	38
3-7 Effect of applying an electric field on the energy states in a semiconductor for a) $E_0=0$ and b) $E_0=\text{finite}$	41
3-8 Electro-absorption for electric fields applied parallel to the plane of the layers in MQW sample, a) 0 V/cm, b) $1.6 \times 10^4$ V/cm, c) $4.8 \times 10^4$ V/cm (after ref. 34)	43

Figure	Page
3-9 Electro-absorption for electric fields applied perpendicular to the plane of the layers in MQW sample, i) $1.6 \times 10^4$ V/cm, ii) $1.3 \times 10^5$ V/cm, iii) $1.8 \times 10^5$ V/cm (after ref. 35)	43
3-10 The effect of an applied electric field on the energy bands and wavefunctions in a quantum well	44
3-11 Photocurrent spectra for a MQW at three different fields. The photocurrent spectrum effectively gives the absorption spectrum of the MQW (after ref. 36)	46
4-1 Cross section of p-i-n diode structure	50
4-2 Room temperature photoluminescence spectrum of $80 \text{ \AA}$ $\text{In}_{0.16}\text{Ga}_{0.84}\text{As}$ / $80 \text{ \AA}$ GaAs MQWs	52
4-3 Schematic diagram of transmission experiment (f=focal length, BS=beamsplitter)	55
4-4 Absorbance spectra as a function of applied electric field	58
4-5 Absorption coefficient as a function of applied electric field	59
4-6 The calculated change in absorption coefficient induced by four different electric field magnitudes	61
A-1 Schematic of photolithographic mask used in the fabrication of the diodes	68

Accession For	
NTIS CRA&I	<input checked="" type="checkbox"/>
DTIC TAB	<input type="checkbox"/>
Unannounced	<input type="checkbox"/>
Justification .....	
By .....	
Distribution /	
Availability Codes	
Dist	Avail and / or Special
A-1	

## List of Tables

Table	Page
4-1 Electric field as a function of applied voltage	60

## List of symbols

$a$	well width
$A$	surface area of diode
$C_{\text{mod}}$	modulator capacitance
$d$	total thickness of multiple quantum well region
$E$	electric field
$E^{2d}$	photon energy
$E_c$	electron energy in conduction band
$E_{\text{gap}}$	energy gap of bulk semiconductor
$E_m^{\text{vb}}$	energy of $m$ th bound hole state in valence band
$E_n^{\text{cb}}$	energy of $n$ th bound electron state in conduction band
$E_o$	incident electric field
$E_r$	reflected electric field
$E_{xy}$	energy in $x, y$ direction
$E_z$	energy in $z$ direction
$E(z)$	total electric field
$E^+(z)$	forward travelling electric field
$E^-(z)$	backward travelling electric field
$f$	focal length of lens
$i$	intrinsic region of diode
$I_o$	transmission intensity through the diode
$I$	transmission intensity through glass slide
$k_x$	electron momentum in $x$ direction

$k_y$	electron momentum in y direction
$L$	etalon cavity thickness
$m$	finesse order number of etalon
$m_b$	electron effective mass in barrier
$m_v$	electron effective mass in well
$m_r$	reduced mass
$M$	transformation components
$n$	n doped region of diode
$n_o$	refractive index
$p$	p doped region of diode
$q$	electron charge
$r$	Fresnel reflection coefficient
$r_j$	interface matrix
$R$	reflectance
$R_1$	front reflectance of etalon
$R_2$	back reflectance of etalon
$t$	Fresnel transmission coefficient
$T$	transmission
$V(z)$	barrier potential
$\alpha$	absorption coefficient
$\alpha_{fc}$	free carrier absorption coefficient
$\beta_j$	layer matrix
$\gamma(z)$	wavefunction in z direction
$\delta$	phase shift in etalon
$\epsilon_o$	free space permitivity

$\epsilon_r$	relative permittivity
$\theta_i$	incident angle in etalon
$\theta_j$	incident angle of electric field in layer matrix
$\lambda_0$	free space wavelength
$\phi(x,y)$	wavefunction in x,y directions
$\psi(x,y,z)$	wavefunction in x,y,z directions
$\omega$	angular frequency
$\hbar$	Plank's reduced constant
$\Delta E_c$	conduction band offset
$\Delta E_v$	valence band offset
$\Delta z$	tilt in conduction band due to electric field

## Chapter 1

### Introduction

High-bandwidth, high-density information processing systems are often limited by electronic bottleneck problems encountered at input/output (I/O) ports.<sup>1</sup> The number of pinouts on VLSI circuits is limited by the crosstalk that can occur between adjacent pins.<sup>2</sup> Optical interconnects have been extensively studied as a possible solution to these problems.<sup>3-6</sup> These optical interconnects are of interest for use in microarea networks ( $\mu$ ANs) for chip to chip and board to board interconnects.

Optical interconnects used in microarea networks can be configured in free space.<sup>7,8</sup> These configurations require very high arrays of on-chip light sources which possess high bandwidth modulation capability. One such source currently being developed is an array of quantum well vertical cavity surface emitting lasers (VCSELs).<sup>9,10</sup> However, the performance of these arrays may be degraded by thermal effects and manufacturing constraints.

An alternative to using large arrays of on-chip lasers is to use a single off-chip laser that could be distributed as an array of beams. These beams would illuminate an array of on-chip modulators. On chip-electronics could then be used to switch the modulators on and off thereby encoding information on an array of continuous wave (CW) laser beams derived from a single source. This optical information could then be routed to another chip for

further processing and eventual conversion back into the electrical domain.

Recent work in developing on-chip electro-optic modulators has focused on using multiple quantum well (MQW) materials as an active medium.<sup>11-14</sup> These devices have been fabricated in both surface normal reflection and waveguide geometries. The reflection modulators are more compatible with chip-to-chip and board-to-board interconnects associated with  $\mu$ ANs. Waveguide geometries are compatible with fiber based interconnects such as those used in local area and wide area distribution networks.

This report describes the fabrication and characterization of strained-layer MQW InGaAs/GaAs layers grown on a GaAs substrate used in the fabrication of an asymmetric Fabry-Perot reflection modulator (ARM) operating at 938 nm. The InGaAs/GaAs material system can be grown in very thin layers so that the lattice mismatch is accommodated by strain rather than misfit dislocations.<sup>15,16</sup> This material system has also been used to make high electron mobility transistors (HEMTs)<sup>17</sup> and avalanche photodiodes.<sup>18</sup> Therefore, it may be possible to integrate electro-optic reflection modulators, transistors and photodiodes all on the same chip.<sup>19</sup> This integration would be very useful in achieving a practical free-space optical interconnect system.

The structure of the ARM is schematically illustrated in Fig.1-1. The ARM is constructed as a p-i-n diode. The p region, which consists of a thin layer of GaAs, forms the front reflector of an asymmetric Fabry-Perot (FP) etalon and has a reflectivity of

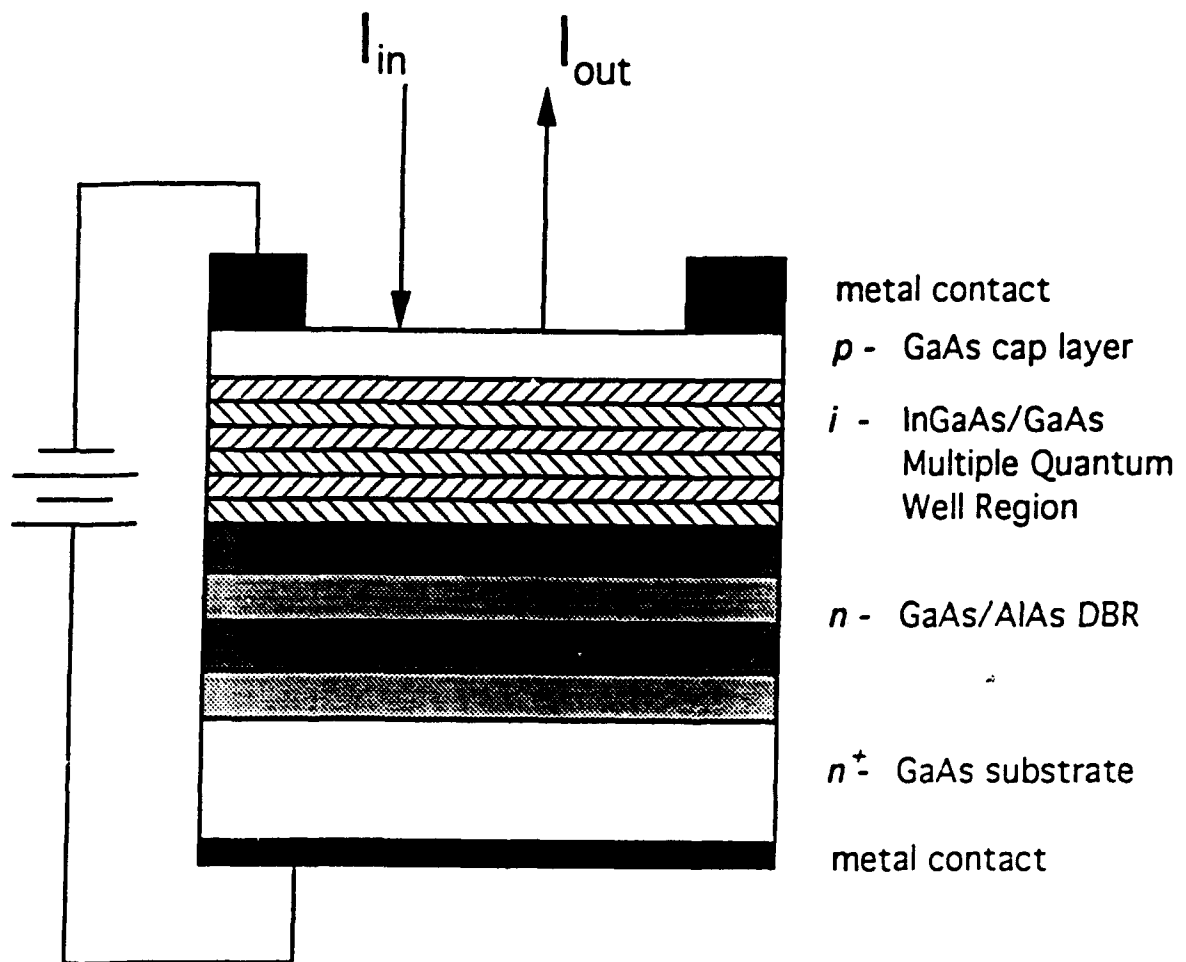


Figure 1-1 Schematic diagram of asymmetric reflection modulator

approximately 0.3. The n region is a highly reflecting distributed Bragg reflector (DBR) and comprises the back reflector of the etalon. The DBR consists of alternating layers of GaAs and AlAs, each a quarter wavelength thick, and has a reflectivity greater than 0.9. An undoped MQW region consisting of strained InGaAs wells and GaAs barriers is placed between the p and n regions and forms the etalon's cavity or spacer region.

Light enters the ARM at normal incidence through the top of the p region. Most of this light passes through the p region into the MQW region, while a small portion of the light is reflected back out. As it passes through the intrinsic region, the light will either be mostly absorbed or mostly transmitted depending upon whether or not an external bias has been applied. The light is then reflected off the back DBR and passes through the MQW region once again before exiting the ARM. If the light was mostly absorbed as it passed through the ARM, then nearly total destructive interference occurs and the initially reflected light is effectively canceled out. Conversely if the ARM passed most of the light back out, very little destructive interference occurs.

The ARM can be described as operating in either the "normally on"<sup>20</sup> or the "normally off"<sup>21</sup> state. In the "normally on" state, the quantum wells are designed so that the modulator is in a high reflectivity state at zero electrical bias. Much of the light that enters the ARM is reflected back out and very little destructive interference occurs. As a bias is applied to the modulator, the absorption edge of the MQW region shifts to longer wavelengths due

to the quantum confined Stark effect (QCSE) and the quantum confined Franz-Keldysh effect (QCFK).<sup>22</sup> The resulting increase in absorption results in a balanced Fabry-Perot cavity and a near zero reflectance of the incident light due to destructive interference. These effects and the change in absorption with applied field will be discussed in detail in Chapter 3.

Conversely, the "normally off" modulator has a near zero reflectance at zero bias. As a bias is applied, the cavity becomes unbalanced, resulting in a high reflectance. The modulator designed in this thesis operates in the "normally off" state.

The electric field required to change the state of the modulator is applied to the MQW region by reverse biasing the diode through contacts applied at the p and n regions. The reverse bias ensures that no excess carriers (i.e. no current) are injected into the diode. The depletion region is contained predominantly within the intrinsic region of the diode. This results in the electric field potential being dropped almost entirely across the MQW region.

The design, development and characterization of the components used in the fabrication of the ARM are investigated more thoroughly in the following chapters. Chapter 2 discusses asymmetric Fabry-Perot theory using an absorptive spacer region and derives the important equations used in the operation and design of the modulator. A matrix formalism is presented as a mathematical method to accurately describe the multiple layer characteristics of the Fabry-Perot etalon. The design and characterization of the

back DBR is also discussed. The optical and electro-optical properties of quantum wells are discussed in Chapter 3. Special emphasis is placed on the quantum confined Stark effect which forms the basis for the modulator operation. The electro-absorption characterization of the MQW region is presented in Chapter 4. The report concludes in Chapter 5 with a design of the ARM. The major findings of this thesis are also summarized in Chapter 5 and possible future directions of the modulator work are suggested.

## Chapter 2

### Asymmetric Fabry-Perot Theory

Fabry-Perot etalons are the basic building block of many modern optical systems. As optical resonators, Fabry-Perot etalons are used to improve the operating characteristics of electro-absorption modulators by increasing the contrast ratio between high and low reflectivity states.<sup>23,24</sup> This chapter discusses etalon operation from two points of view. First, single layer theory will be presented for asymmetric etalons. A matrix formalism will then be used to account for the multiple layers that are actually found in optical reflection modulators.

#### 2.1 Single layer theory

Fabry-Perot etalons are formed by two plane, parallel, partially reflecting mirrors separated by a medium of thickness  $L$  and index of refraction  $n$ . The etalon is symmetric when the front and back mirrors have the same reflectivities. Conversely, etalons are considered asymmetric when the two reflectivities are different. Single film non-absorbing etalons have been examined in detail in many optical textbooks.<sup>25</sup> However, this section derives the general operating equations for an asymmetric etalon with an absorbing spacer region.

The etalon's reflection and transmission characteristics can be analyzed by considering the effects of an infinite number of

plane waves being reflected by the two mirrors. As shown in Fig. 2-1a, an electric field,  $E_0$  is incident upon mirror 1,  $M_1$ , at angle  $\theta_i$ . The amplitudes of the reflected waves  $E_{r1}$ ,  $E_{r2}$ ,  $E_{r3}$ , ..., are given by  $E_0 r_1$ ,  $E_0 t_1 t_1' r_2'$ ,  $E_0 t_1 t_1' r_1' r_2'^2$ , ..., where the  $r$ 's and  $t$ 's are the Fresnel reflection and transmission coefficients of the respective surfaces.

The total electric field reflected by the etalon is found by summing the infinite number of reflected waves,  $E_{r1}$ ,  $E_{r2}$ , ...,  $E_{rn}$ . The transmission of the etalon is calculated in the same manner by summing the infinite number of transmitted waves through the second reflector,  $E_{t1}$ ,  $E_{t2}$ , ...,  $E_{tn}$ .

The sum of reflected waves from the etalon is given by

$$E_r = E_0 [r_1 + t_1 t_1' r_2' \exp(j\delta) + t_1 t_1' r_1' r_2'^2 \exp(j2\delta) + t_1 t_1' r_1'^2 r_2'^3 \exp(j3\delta) + \dots], \quad (2.1)$$

where  $\delta$  is the phase shift resulting from the optical path length difference between two adjacent reflected waves.

This round trip phase shift can be derived using Fig. 2-1b. The phase shift between two successive reflected waves at the first reflector is found from the path length difference between these two waves,  $\Delta l$ .

$$\Delta l = AB + BC. \quad (2.2)$$

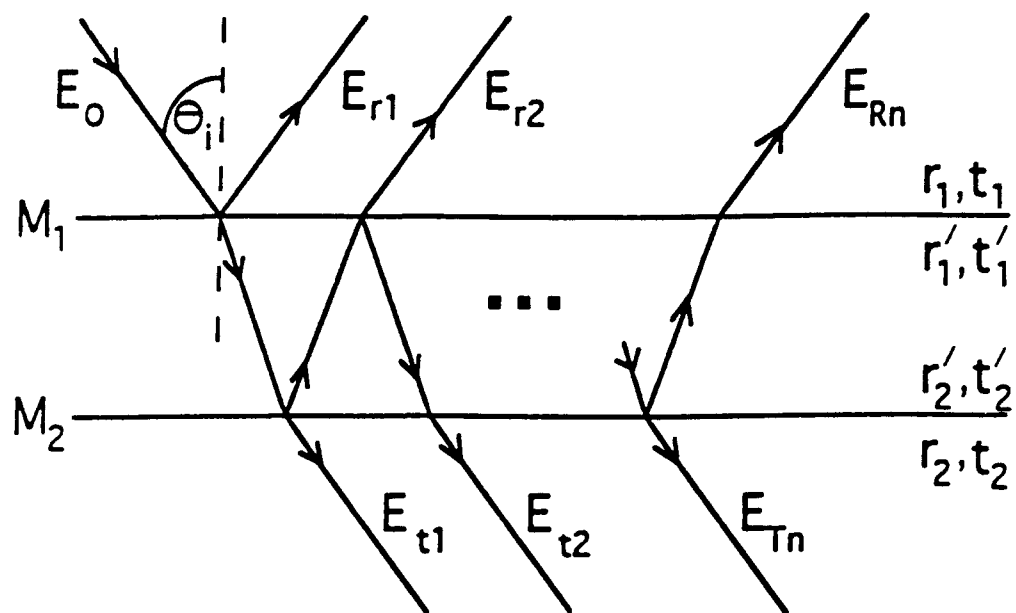


Figure 2-1a Single layer asymmetric Fabry-Perot etalon

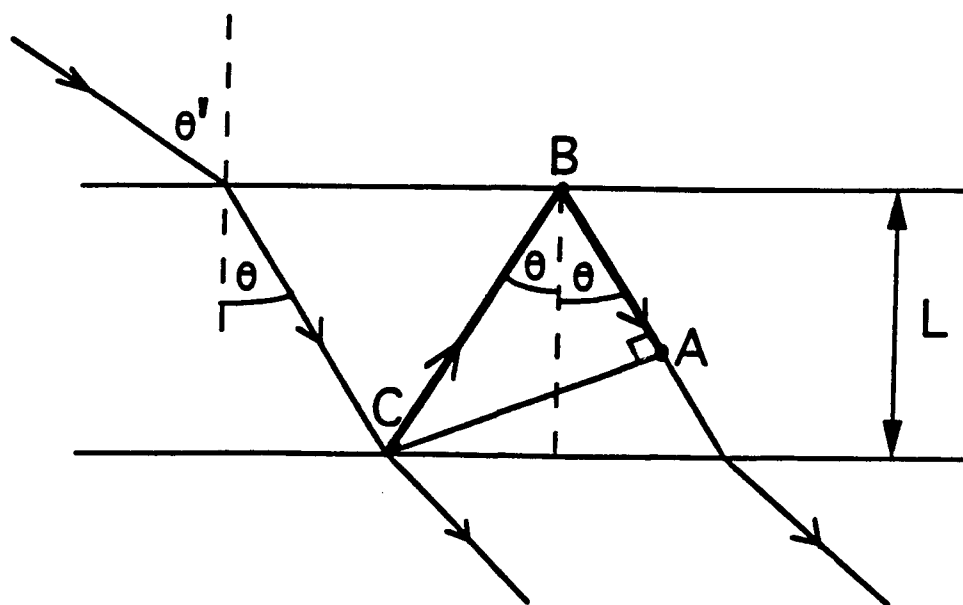


Figure 2-1b Round trip phase shift in Fabry-Perot etalon

The path lengths AB and BC are given by

$$AB = \frac{L}{\cos\theta} \cdot \cos 2\theta \quad (2.3)$$

and

$$BC = \frac{L}{\cos\theta} \cdot \quad (2.4)$$

Substituting Eqs. (2.3) and (2.4) into Eq. (2.2),

$$\Delta l = \frac{L \cos 2\theta}{\cos\theta} + \frac{L}{\cos\theta} = \frac{L}{\cos\theta} [1 + \cos 2\theta] \cdot \quad (2.5)$$

Using trigonometric identities, Eq. (2.5) reduces to

$$\Delta l = 2L \cos\theta. \quad (2.6)$$

The phase shift  $\delta$  is defined as

$$\delta = k \Delta l = \frac{2\pi n}{\lambda_o} \Delta l, \quad (2.7)$$

where  $k$  is the propagation constant within the etalon and  $\lambda_o$  is the free space wavelength. Substituting Eq. (2.6) into Eq. (2.7) the round trip phase shift is given by

$$\delta = \frac{4\pi n L \cos\theta}{\lambda_o} \cdot \quad (2.8)$$

The common terms in Eq. (2.1) can be factored out of the expression resulting in

$$E_r = E_o \{ r_1 + t_1 t_1' r_2' \exp(j\delta) [1 + r_1' r_2' \exp(j\delta) + r_1' r_2' \exp(j2\delta) + \dots] \} \quad (2.9)$$

The terms within the square brackets form an infinite geometric series which reduces Eq. (2.9) to

$$E_r = E_o \left[ \frac{r_1 + r_2' \exp(j\delta)}{1 - r_1' r_2' \exp(j\delta)} \right]. \quad (2.10)$$

The phase term given by Eq. (2.8) can be rewritten in the form

$$\delta = \delta_o + j\alpha L, \quad (2.11)$$

where  $\alpha$  is the absorption coefficient of the spacer material and  $\delta_o = 4\pi n_o L \cos\theta / \lambda$ . Substituting Eq. (2.11) into Eq. (2.10) results in

$$E_r = E_o \left[ \frac{r_1 + r_2' \exp(j\delta_o) \exp(-\alpha L)}{1 - r_1' r_2' \exp(j\delta_o) \exp(-\alpha L)} \right]. \quad (2.12)$$

The reflectance of the etalon,  $R$ , is found by multiplying Eq. (2.12) by its complex conjugate,  $E_r^*$  and then dividing by the incident intensity,  $E_o E_o^*$ .

$$R = \left| \frac{E_r}{E_o} \right|^2 = \frac{[r_1 + r_2' \exp(j\delta_o)] [r_1 + r_2' \exp(-j\delta_o)]}{[1 - r_1' r_2' \exp(j\delta_o)] [1 - r_1' r_2' \exp(-j\delta_o)]}. \quad (2.13)$$

After multiplying the terms out and using the identity,

$$\cos \delta_o = \frac{\exp(j\delta_o) + \exp(-j\delta_o)}{2}, \quad (2.14)$$

Eq. (2.13) simplifies to

$$R = \frac{r_1^2 + r_2^2 \exp(-2\alpha L) + 2r_1 r_2' \exp(-\alpha L) \cos \delta_o}{1 + r_1^2 \exp(-2\alpha L) + 2r_1' r_2' \exp(-\alpha L) \cos \delta_o}. \quad (2.15)$$

The identity  $\cos \delta_o = (1 - \sin^2 \delta_o / 2)$  and the definitions,  $r_1 = -r_1'$ ,  $r_2 = -r_2'$ ,  $R_1 = r_1^2 = r_1'^2$ ,  $R_2 = r_2^2 = r_2'^2$  are used to give the final expression for the reflectance of the etalon.

$$R = \frac{(\sqrt{R_1} - \sqrt{R_2} \exp(-2\alpha L))^2 + 4\sqrt{R_1 R_2} \exp(-2\alpha L) \sin^2 \frac{\delta_o}{2}}{(1 - \sqrt{R_1 R_2} \exp(-2\alpha L))^2 + 4\sqrt{R_1 R_2} \exp(-2\alpha L) \sin^2 \frac{\delta_o}{2}}. \quad (2.16)$$

The reflectance of the Fabry-Perot etalon will be at a minimum whenever the term  $\sin^2 \delta_o / 2$  equals zero. This occurs whenever

$$\delta_o = \frac{4\pi n_o L \cos \theta}{\lambda_o} = 2m\pi, \quad (2.17)$$

where  $m$  is defined as the order number of the etalon and is any integer,  $m = \pm 1, \pm 2, \dots$ , etc. Assuming the incident light is normal to the etalon, Eq. (2.17) simplifies to

$$L = \frac{m\lambda_o}{2n_o}. \quad (2.18)$$

When this condition is satisfied, the etalon is said to be at resonance and results in a minimum reflectance. As Eq. (2.18) suggests this condition is satisfied whenever the cavity thickness is an integer number of half wavelengths. Thus, the minimum reflectance in a lossy etalon at resonance is

$$R = \left[ \frac{\sqrt{R_1} - \sqrt{R_2} \exp(-2\alpha L)}{1 - \sqrt{R_1 R_2} \exp(-2\alpha L)} \right]^2. \quad (2.19)$$

Recall that in a lossless cavity, the reflectance at resonance is zero if the front and back mirrors have the same reflectivities. However, considering losses, Eq. (2.19) shows that the reflectance at resonance will only be zero when

$$R_1 = R_2 \exp(-2\alpha L). \quad (2.20)$$

Using Eq. (2.19), a plot of reflectance as a function of  $2\alpha L$  is shown in Fig. 2-2. In this plot, the values  $R_1=0.3$  and  $R_2=0.9$  were used for the reflectances of the front and back mirror, respectively. These values are very close to the reflectivities used for the design of the reflection modulator used in this work. Fig. 2-2 shows that a small change in the absorption coefficient for  $2\alpha L < 1$  will result in a rather large change in the reflectance. This property is extremely useful in the design of an electro-absorption reflection modulator, where  $\alpha$  is a function of applied electric field,  $\alpha=\alpha(E)$ .

This section has derived the basic equations for an

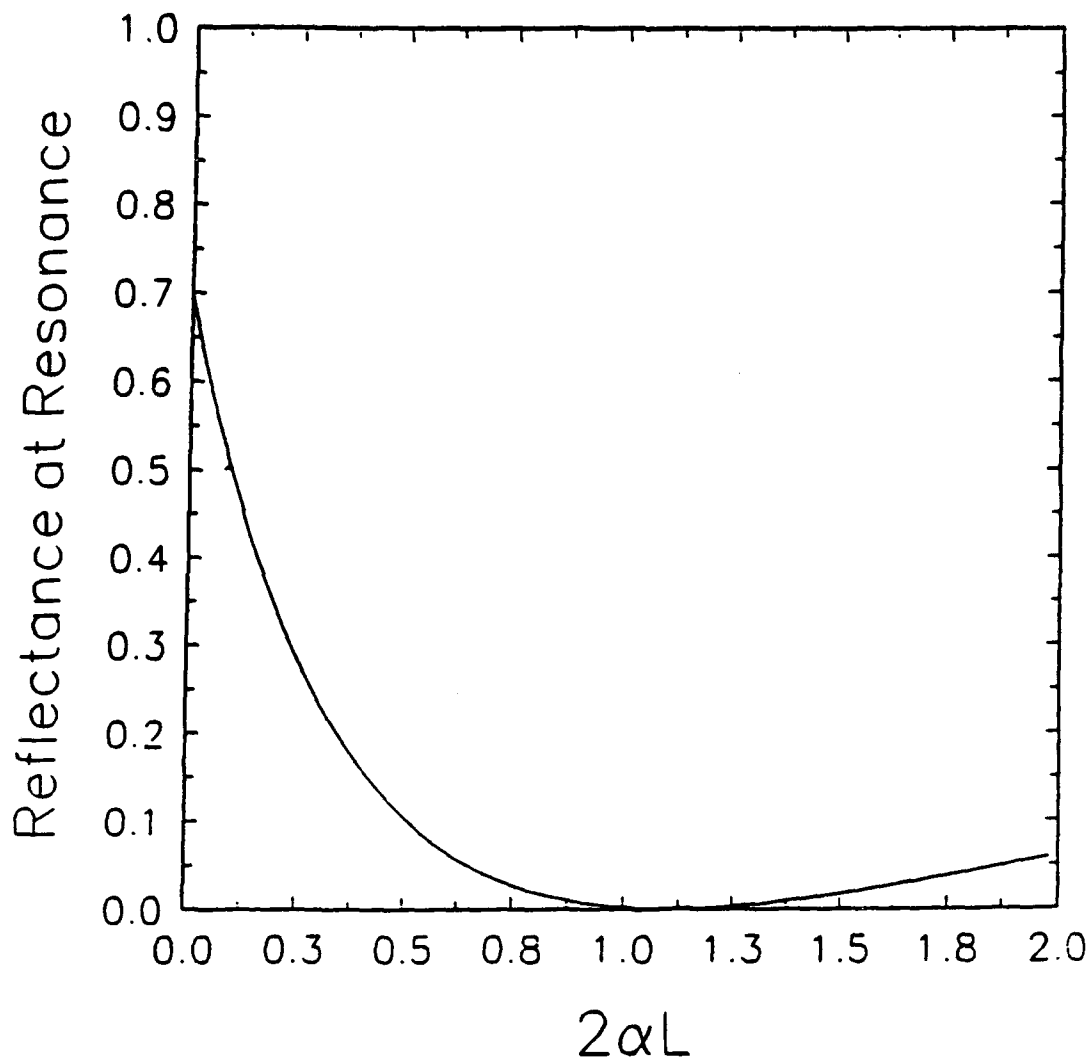


Figure 2-2 Reflectance at resonance versus spacer absorbance for a single layer etalon

asymmetric Fabry-Perot etalon. These equations are valid for an ideal system in which the mirrors and cavity are all composed of single layer materials. The next section develops the effects of multiple layers on the operation of an etalon as a resonant system.

## 2.2 Multiple layer theory

Since the ARM structure requires the use of many layers of semiconductor materials, a calculation of the etalon's reflectance using ray tracing techniques would be quite cumbersome, indeed. For this purpose, matrix techniques are a convenient method for calculating the reflection and transmission coefficients associated with multiple layer structures.<sup>26</sup> The following matrix formalism is used to accurately calculate the reflectance and model the Fabry-Perot effects of this modulator. Therefore, this is a very useful tool in the design process of the ARM.

Following the formalism of Vigoureaux, the complex electric field amplitudes of a forward and backward travelling wave in the  $z$  direction can be denoted by  $E^+[z]$  and  $E^-[z]$  respectively. The total electric field is then represented by a  $2 \times 1$  matrix, thus:

$$E(z) = \begin{bmatrix} E^+(z) \\ E^-(z) \end{bmatrix}. \quad (2.21)$$

The fields at the  $z'$  and  $z''$  planes, with wavefronts parallel to the plane boundaries, are related by a  $2 \times 2$  matrix transformation  $M$ . This transformation is given by

$$\begin{bmatrix} E_1^+(z') \\ E_1^-(z'') \end{bmatrix} = \begin{bmatrix} M_{11} & M_{12} \\ M_{21} & M_{22} \end{bmatrix} \begin{bmatrix} E_n^+(z'') \\ E_n^-(z'') \end{bmatrix}, \quad (2.22)$$

where 1 and n denote the first and nth layers, respectively. As can be seen in Eq. (2.22), the reflection and transmission coefficients are directly related to [M]. Taking  $E_n^-(z)$  as zero when n is the last layer of the structure so the reflection and transmission coefficients are expressed as

$$\mathcal{R}_n = \frac{E_1^-(z)}{E_1^+(z)} = \frac{M_{21}}{M_{11}} \quad (2.23)$$

and

$$\mathcal{T}_n = \frac{E_n^+(z)}{E_1^+(z)} = \frac{1}{M_{11}}. \quad (2.24)$$

The matrix [M] is the product of two matrices,  $[M] = [r][\beta]$ . The interface matrix  $[r_j]$  describes the reflection and transmission of the fields at the  $(j, j+1)$  interface and is defined as  $E(z_j - \epsilon) = [r_j]E(z_j + \epsilon)$ . When  $\epsilon \rightarrow 0$  the interface matrix is given by

$$[r_j] = \frac{1}{t_{j,j+1}} \begin{bmatrix} 1 & r_{j,j+1} \\ r_{j,j+1} & 1 \end{bmatrix}. \quad (2.25)$$

In Eq. (2.25),  $r_{j,j+1}$  and  $t_{j,j+1}$  are the Fresnel reflection and transmission coefficients at the  $(j, j+1)$  interface.

The layer matrix  $[\beta_j]$  describes the phase shift and

attenuation of the field as it travels through the  $j$ th layer. It is defined as  $E(z_j + \epsilon) = [\beta_j]E(z_j + d_j + \epsilon)$ , where  $\epsilon$  is infinitely small and  $d_j$  is the thickness of the  $j$ th layer. The layer matrix is given by

$$[\beta_j] = \begin{bmatrix} \exp i\beta_j & 0 \\ 0 & \exp -i\beta_j \end{bmatrix}. \quad (2.26)$$

The  $\beta_j$  terms contained within the matrix represents the phase shift of the field as it propagates through the layer and is defined as

$$\beta_j = \frac{2\pi}{\lambda_o} n_j \cos \theta_j (z_j - z_{j-1}). \quad (2.27)$$

In Eq. (2.27),  $\theta_j$  is the incident angle of the electric field and  $n_j$  is the index of refraction within the medium. The index of refraction is complex if the medium is lossy and is given by

$$n_{c,j} = n_o + i \frac{\alpha \lambda_o}{4\pi}, \quad (2.28)$$

where  $n_o$  denotes the real part of the index and  $\alpha$  is absorption coefficient of the medium for wavelength  $\lambda_o$ . Substituting Eq. (2.28) into Eq. (2.27),  $\beta_j$  now includes the attenuation of the field as well as the phase change resulting in

$$\beta_j = \frac{2\pi}{\lambda} n_{o,j} (z_j - z_{j-1}) + i \left( \frac{\alpha}{2} \right) (z_j - z_{j-1}). \quad (2.29)$$

The transformation matrix,  $[M_n]$  for the  $n$ -layer system is

completely described by

$$[M_n] = [r_1] [\beta_1] [r_2] [\beta_2] [r_3] [\beta_3] \dots [r_n] [\beta_n]. \quad (2.30)$$

Since the layer matrix is complex, the reflectance of the system is given by

$$\mathfrak{R} = \frac{E_1^-(z)}{E_1^+(z)} = \left| \frac{M_{21}}{M_{11}} \right|^2. \quad (2.31)$$

The matrix multiplication encountered in Eq. (2.30) can be quite cumbersome to evaluate when there are more than 2 or 3 layers. Therefore, a C computer program was written which evaluates Eq. (2.31).<sup>27</sup> This program calculates the reflectance of an asymmetric Fabry-Perot structure with a distributed Bragg reflector (DBR) as the back mirror.

To illustrate the usefulness of this technique as a design tool, Fig. 2-3 shows the reflectance spectrum of a DBR centered at 950 nm for both 10 and 15 periods of the GaAs/AlAs material system. This is the actual DBR material system that is used in the design of the ARM in this work. As the number of periods of the DBR increases, the peak reflectivity increases, but the spectral bandwidth decreases. This is an important design tradeoff which must be considered when designing the reflection modulator. Calculations using this program will be discussed in the next section as they pertain to the design and characterization of an actual DBR which could be incorporated into a reflection modulator.

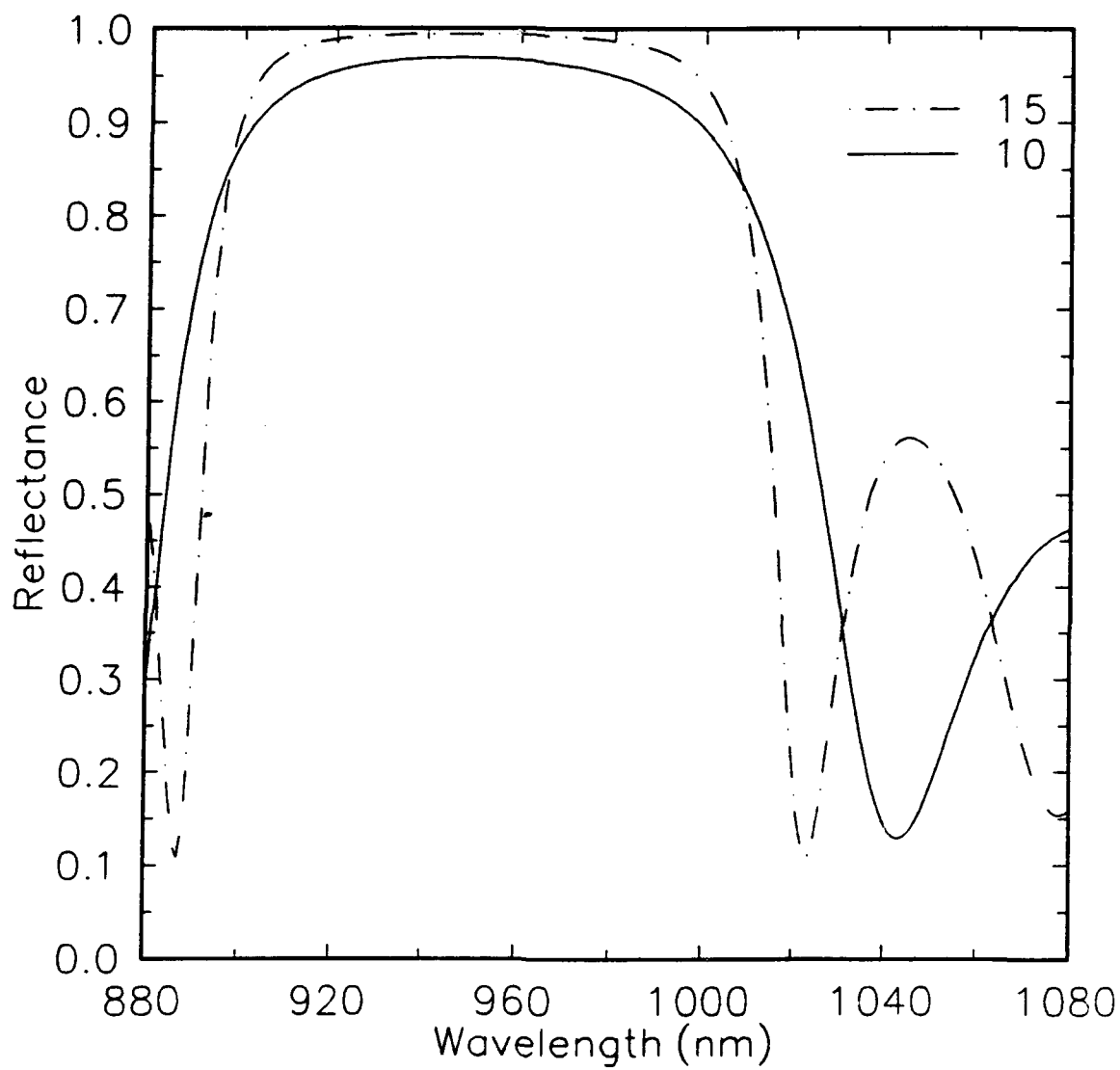


Figure 2-3 Calculated reflectance spectrum for 10 and 15 period distributed Bragg reflectors

### 2.3 Design, growth and characterization of GaAs/AlAs DBR

A highly reflecting distributed Bragg reflector can easily be fabricated using a relatively small number of periods of the GaAs/AlAs material system. This is the result of the difference in the refractive indices of the two materials being relatively large. If this difference were small, then a large number of periods would be need to achieve a very high reflectance.

The refractive index of GaAs as a function of wavelength is given by<sup>28</sup>

$$n^2 = 1 + \frac{A}{\pi} \ln \left[ \frac{E_1^2 - (\hbar\omega)^2}{E_o^2 - (\hbar\omega)^2} \right] + \frac{G_1}{E_1^2 - (\hbar\omega)^2} + \frac{G_2}{E_2^2 - (\hbar\omega)^2} + \frac{G_3}{E_3^2 - (\hbar\omega)^2} \quad 2.32$$

where

$$\begin{aligned} E_o &= 1.428 \text{ eV} \\ E_1 &= 3.0 \text{ eV} \\ E_2 &= 5.1 \text{ eV} \\ E_3 &= 0.0333 \text{ eV} \\ G_1 &= 39.194 \text{ eV}^2 \\ G_2 &= 136.08 \text{ eV}^2 \\ G_3 &= 0.00218 \text{ eV}^2 \\ A &= 0.5858 \\ \text{and } \hbar\omega &= \text{the photon energy} \end{aligned}$$

The refractive index of AlAs as a function of wavelength is given by<sup>29</sup>

$$n^2 = 1 + \frac{E_o E_d}{E_o^2 - (\hbar\omega)^2} \quad (2.33)$$

where

$$\begin{aligned} E_o &= 4.70 \\ E_d &= 33.65. \end{aligned}$$

A fifteen period 69 nm GaAs/ 82 nm AlAs DBR centered at 970 nm was grown on a GaAs substrate by molecular beam epitaxy (MBE)<sup>30</sup>. Transmission measurements were then used to characterize the DBR. The DBR is non-absorbing in the wavelength region of interest, i.e. 900 nm through 1000 nm. Therefore, the reflectance of the DBR is given by

$$R=1-T, \quad (2.34)$$

where  $R$  is the reflectance of the DBR and  $T$  is the measured transmission through the DBR. The experimental setup used to measure the transmission is described in detail in Section 4.2.

Fig. 2-4 shows the measured reflectance spectrum (dotted spectrum) and the theoretical fit (solid line) for the DBR with a center wavelength of 970 nm. The theoretical fit shows good agreement with the actual DBR especially in the high reflectance center wavelength region. The spectrum could only be measured out to 1015 nm due to the limitations of the detector. This measurement shows that a reflectance of greater than 99% can be achieved with as few as 15 periods. The spectral bandwidth of this DBR is approximately 100 nm. The high reflectivity of this DBR over a wide range makes it ideal for use as the back reflector of the ARM.

In summary, this chapter has derived the basic equations governing the operation of an asymmetric Fabry-Perot etalon. These

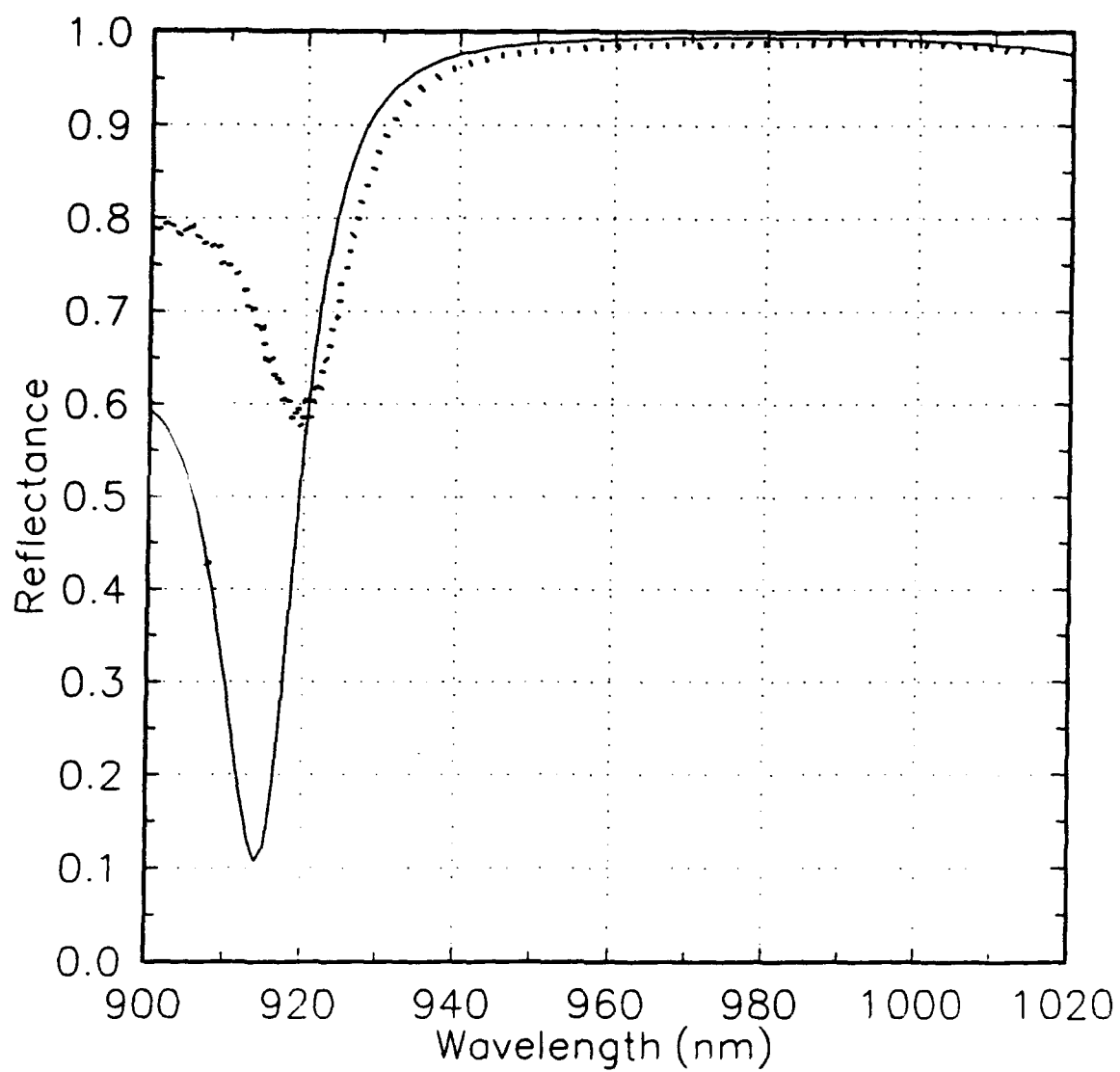


Figure 2-4 Measured reflectance spectrum of 15 period GaAs/AlAs DBR

equations are very important in describing the basic operation of the etalon structure. Next, a matrix formalism was developed to calculate the reflectance of a multi-layer structure and thus accurately model the characteristics of an asymmetric Fabry-Perot etalon device with an absorbing spacer region. As will be seen, the use of the matrix formalism becomes an important design tool in assessing tradeoffs in the characteristics of the etalon structure to achieve an optimal design. A fifteen period GaAs/AlAs DBR was also characterized. The high reflectance of this DBR over a large spectral bandwidth makes it suitable for use as the back reflector of the ARM.

## Chapter 3

### Optical and Electro-optical Properties of Quantum Well Structures

Semiconductor growth techniques, such as molecular beam epitaxy (MBE), have experienced considerable advancements in recent years. These improved techniques have made it possible to grow ultrathin semiconductor films of high quality and high reproducibility. Film thicknesses of this order ( $d \leq 100 \text{ \AA}$ ) can lead to a reduction in the dimensionality of the semiconductor system and make possible the growth of semiconductor quantum well structures. Furthermore, by controlling these thicknesses the quantum well can have its optical properties tailored to meet system requirements. This chapter describes the optical and electro-optical properties of semiconductor quantum well structures which are attractive for use in asymmetric Fabry-Perot reflection modulators.

#### 3.1 Quantum well theory

Quantum wells are composed of a very thin layer of narrow energy bandgap semiconductor material surrounded by a wider energy bandgap semiconductor material as shown in Fig. 3-1. The wide gap material forms the barriers and the narrow gap material forms the wells. Quantum wells are described as being quasi-two dimensional because electrons are confined in the plane of the well or

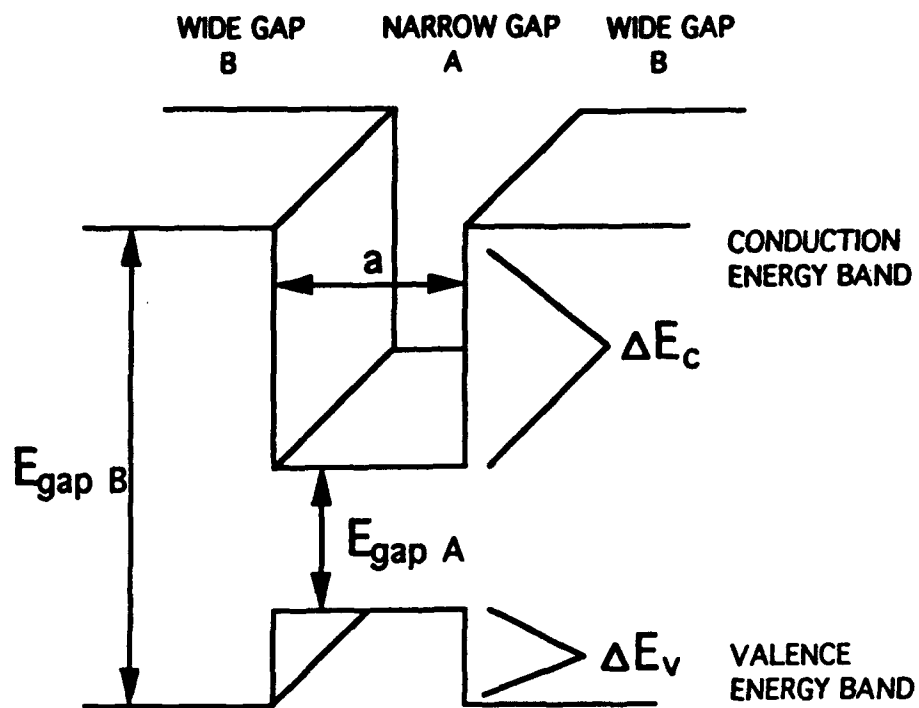


Figure 3-1 Schematic band structure for a single quantum well

z - direction, but free to move in a continuum in the plane perpendicular to the well, i.e. the x - y direction. The confinement in the z-direction results in a set of discrete energy levels. The quantum well is then analogous to the quantum mechanics problem of the particle in the box. The energy level transitions that can occur in quantum wells can be tailored to meet system requirements. For example, the bandedge in the  $\text{In}_x\text{Ga}_{1-x}\text{As}/\text{GaAs}$  system can be tuned by adjusting the thickness of the InGaAs layers and to some extent by adjusting the alloy compositions or mole fraction x of the InGaAs material.

The band gap difference formed by the combination of the barrier and well materials forms a square well with finite potential as illustrated in Fig. 3-1. For the well material, the discrete energy levels E in both the conduction and valance bands are calculated using the time-independent Schrödinger equation which is given as

$$\nabla^2 \psi(x, y, z) + \frac{2m}{\hbar^2} [E - V(x, y, z)] = 0, \quad (3.1)$$

where  $\hbar$  is Plank's reduced constant, m is the mass of the particle, and V is the potential of the barrier. The wavefunction  $\psi(x, y, z)$  for the system is written as a product of wavefunctions for the x-y and z directions

$$\psi(x, y, z) = \phi(x, y) \gamma(z), \quad (3.2)$$

where  $\phi(x, y)$  is the wavefunction of the electron in the x-y plane

and  $\gamma(z)$  is the wavefunction of the electron confined in the  $z$ -direction. The Schrödinger equation can now be separated into two equations

$$\left[ \frac{\partial^2}{\partial x^2} + \frac{\partial^2}{\partial y^2} \right] \phi(x, y) + \frac{2m}{\hbar^2} E_{xy} \phi(x, y) = 0, \quad (3.3)$$

which describes the motion of the electron in the  $xy$  direction and

$$\frac{\partial^2}{\partial z^2} \gamma(z) + \frac{2m}{\hbar^2} [E_z - V_z] = 0. \quad (3.4)$$

which describes the motion of the electron in the  $z$ -direction.

The potential energy is defined as zero in the  $x$ - $y$  plane because the electron is free to move in a continuum. Within the well however, the barrier potential  $V(z)$  is defined as

$$V(z) = \begin{cases} 0 & -\frac{a}{2} < z < \frac{a}{2} \\ V_z & |z| > \frac{a}{2} \end{cases} \quad (3.5)$$

Eq. (3.3) has solutions in the form of plane waves

$$E_{xy} = \frac{\hbar^2}{2m} [k_x^2 + k_y^2], \quad (3.6)$$

where  $k_x$  and  $k_y$  are the electron momentum values in the  $x$  and  $y$  directions.

Eq. (3.4) has solutions in the form of the following two transcendental equations

$$\tan\left[\left(\frac{m_w a^2 E_z}{2\hbar^2}\right)^{\frac{1}{2}}\right] = \sqrt{\frac{m_w}{m_b} \left(\frac{V_z}{E_z} - 1\right)} \quad (3.7)$$

and

$$-\cot\left[\left(\frac{m_w a^2 E_z}{2\hbar^2}\right)^{\frac{1}{2}}\right] = \sqrt{\frac{m_w}{m_b} \left(\frac{V_z}{E_z} - 1\right)}, \quad (3.8)$$

where  $m_w$  is the effective mass of the electron in the well,  $m_b$  is the effective mass of the electron in the barrier, and  $a$  is the width of the well. Eq. (3.7) has even bound state energy solutions and Eq. (3.8) has odd bound state energy solutions. The solution of Eqs. (3.7) and (3.8) result in discrete energies  $E_z$  within the well. This energy can be written as  $E_n$ , where  $n$  denotes the quantum number of the  $n$ th discrete or quantized state.

The energy of an electron in a quantum well can now be fully described. Assuming that the zero of energy is taken as the top of the valence band, the energy of the electron in the conduction band of the quantum well is given by

$$E_c = E_{gap} + \frac{\hbar^2}{2m} [k_x^2 + k_y^2] + E_n^{cb}, \quad (3.9)$$

where  $E_{gap}$  is the energy gap of the bulk semiconductor material and  $E_n^{cb}$  is the  $n$ th bound state in the conduction band.

The dispersion relations, energy versus momentum relations resultant from a plot of Eq. (3.9), are shown in Fig. 3-2. The dispersion relation for the bulk semiconductor is denoted by the

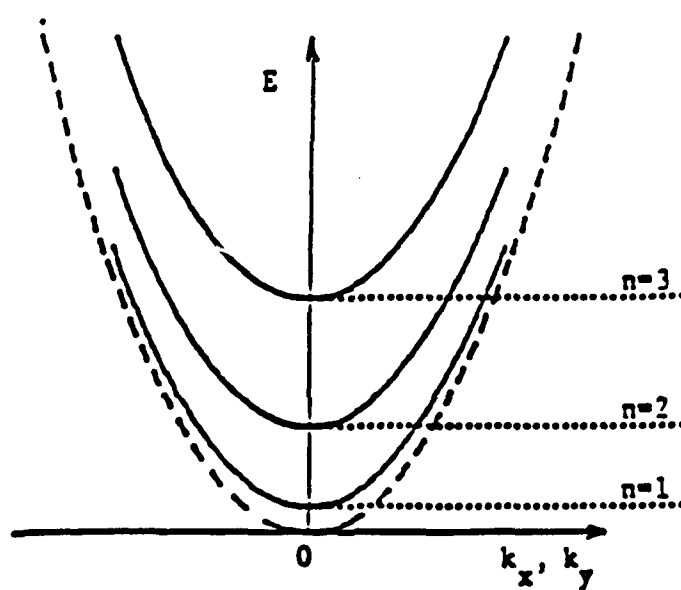


Figure 3-2 The dispersion relation, Energy versus  $k_{x,y}$ , in momentum space for bulk semiconductor (dashed line) and a single quantum well (solid line)

dashed line. As seen in this figure, each subband is displaced from the bulk energy value by an amount equal to  $E_n$ . These values of  $E_n$  correspond to the allowed energy states in the z-direction within the quantum well. The amount of displacement from the bulk value can be controlled by changing the value of the well width  $a$ , as evident in Eqs. (3.7) and (3.8). Therefore, the effective bandgap of quantum well materials can be altered by simply changing the thickness of the well material. This is known as the quantum size effect and has many useful device applications.

In a quantum well, the minimum photon energy required to promote an electron from the valance band to the conduction band is given by

$$E^{2d} = \hbar\omega = E_{gap} + E_n^{cb} - E_m^{vb} + \frac{\hbar^2}{2m_r} [k_x^2 + k_y^2], \quad (3.10)$$

where  $E_n^{cb}$  is the  $n$ th bound electron state in the conduction band,  $E_m^{vb}$  is the  $m$ th bound hole state in the valance band and  $m_r$  is the reduced mass of the system. The only allowed transition occurs when  $n = m$ . For example, selection rules state that the transition from  $E_1^{cb}$  to  $E_1^{vb}$  is the lowest allowed transition that can occur. For  $n \neq m$ , the transition cannot occur because the electron and hole envelope wavefunctions are nearly orthogonal.

For direct bandgap materials, the maximum point in the valence band and the minimum point in the conduction band occur at the  $\Gamma$  point, i.e.  $k_x = k_y = 0$ . This is the point at which the lowest allowed optical transition occurs ( $n=m=1$ ). The photon energy in a

quantum well is now given by

$$E_1^{2d} = \hbar\omega = E_{gap} + E_1^{cb} + E_1^{vb}. \quad (3.11)$$

Fig. 3-3 shows a plot of Eq. 3.11 as a function of well width for an  $\text{In}_{.52}\text{Al}_{.48}\text{As}/\text{In}_{.53}\text{Ga}_{.47}\text{As}/\text{In}_{.52}\text{Al}_{.48}\text{As}$  quantum well. However, the functional relationship between the absorption coefficient bandedge and the well width is valid for all quantum well systems. As the width of the InGaAs well is increased, the bandgap energy decreases and approaches the bandgap energy of bulk InGaAs (0.76 eV). If the width of the InGaAs quantum well is made narrow enough, the photon energy approaches the bandgap energy of the InAlAs barrier material (1.46 eV).

This section has discussed some of the properties of quantum well systems that distinguish them from bulk material systems. Specifically, the idea of the quantum size effect has been introduced. This effect allows the optical properties of multiple quantum well systems to be tailored to meet the needs of the system. The next section discusses the absorption properties of quantum well systems and how these properties are affected by coulombic interactions.

### 3.2 Optical absorption properties of quantum wells

The free carrier absorption coefficient  $\alpha_{fc}$  in quantum wells is proportional to the joint density of states.<sup>31</sup> This relationship

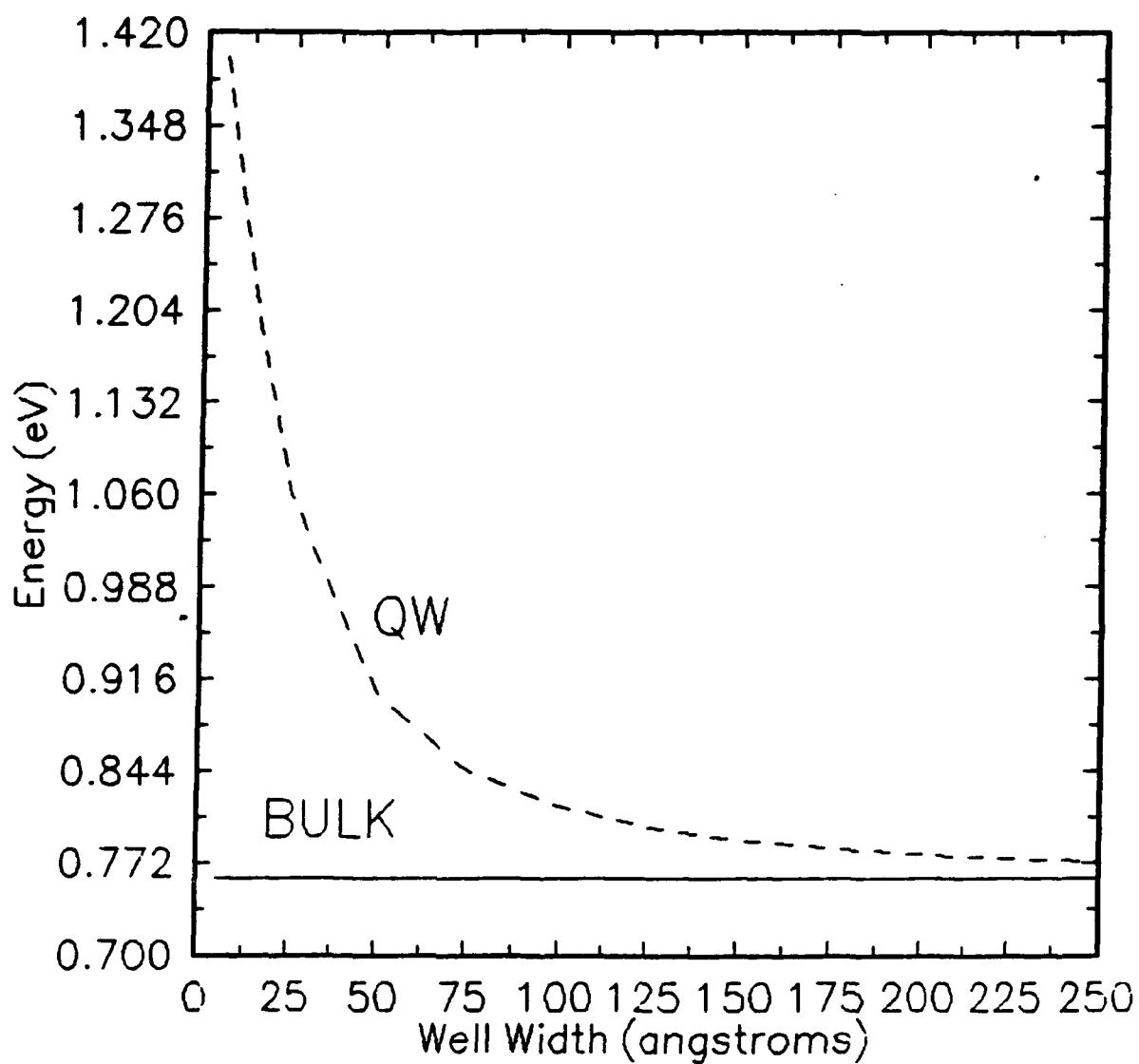


Figure 3-3 Well width dependence of the first allowed transition of a single quantum well

is shown as

$$\alpha_{fc}(\omega) \propto \frac{m_r}{\pi \hbar^2} \sum_{m,n} U_{-1}(\hbar\omega - E_g - E_m^{cb} - E_n^{vb}), \quad (3.12)$$

where  $m_r$  is the reduced mass of the electron-hole pair defined as  $m_r = m_e m_h / (m_e + m_h)$ ,  $E_g$  is the bulk bandgap energy for the system and  $E_{m,n}^{cb,vb}$  are the confined energy states for the electrons and holes, respectively.  $U_{-1}(\hbar\omega - E_g - E_m^{cb} - E_n^{vb})$  is a step function which makes the free carrier absorption spectra resemble a stair case like function with steps at equal values of  $m$  and  $n$  as shown in Fig. 3-4. The absorption has a non-zero value at the lowest photon transition energy. This is an important feature of reduced dimensionality systems.

In semiconductors, an attractive coulombic potential exists between the negatively charged electron and the positively charged hole created by the absorption of a photon. This bound electron-hole pair forms a hydrogen-like atom known as an exciton. The coulombic potential has a large effect on the absorption coefficient and its effect must be included.

The energy of the  $n = m = 1$  exciton is displaced from the 2-d photon energy of the quantum well by the 2-d excitonic binding energy

$$E_1^{exciton} = E_1^{2d} - E_b^{2d} \quad (3.13)$$

The last term in Eq. (3.13) is the 2-d binding energy of the

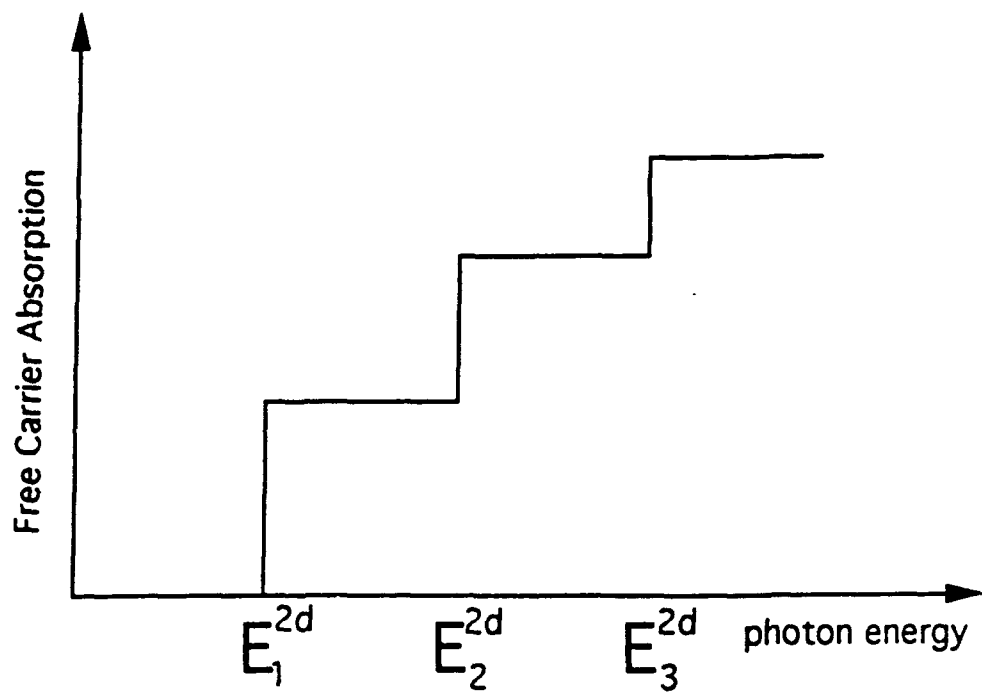


Figure 3-4 Optical free carrier absorption spectrum of a single quantum well

exciton  $E_b^{2d}$  and is equal to<sup>31</sup>

$$E_B = \frac{q^4 m_r}{8\pi\epsilon_r\epsilon_0\hbar^2\left(n - \frac{1}{2}\right)^2}, \quad (3.14)$$

where  $\epsilon_r$  is the relative permittivity of the medium and  $\epsilon_0$  is the free space permittivity.

The absorption coefficient which now includes the coulombic effects is given by the 2-d Elliot formula as<sup>31</sup>

$$\alpha^{2-d}(\omega) = \frac{2\pi\omega |d_{cv}|^2}{n_0 c a} \left( \frac{2m_r}{\hbar^2} \right) \left[ \sum_{n=1}^{\infty} \frac{4E_B}{\left(n - \frac{1}{2}\right)^3} \delta\left(\hbar\omega - E_g^{2-d} + \frac{E_B}{\left(n - \frac{1}{2}\right)^2}\right) + U_{-1}(\hbar\omega - E_g^{2-d}) \frac{e^{\Delta}}{\cosh\Delta} \right] \quad (3.15)$$

where

$$\Delta = \frac{\pi}{\sqrt{\frac{\hbar\omega - E_g^{2-d}}{E_B}}}. \quad (3.16)$$

The first term in brackets in Eq. (3.15) corresponds to the excitonic absorption lines at positions  $\hbar\omega = E_g + E_m^{cb} - E_b/(n-1/2)^2$ . The magnitude of these excitonic lines is proportional to  $1/(n-1/2)^3$ . The second term in the brackets is the Coulomb enhanced absorption continuum. This enhanced absorption effect results in the absorption coefficient at the bandedge being twice as large as

the 2-d free-carrier absorption coefficient. Fig. 3-5 shows a comparison between the free carrier and excitonic absorption spectra. The dashed lines show the free carrier absorption spectra and the solid lines show the excitonic absorption spectra.

The absorption spectrum of an  $\text{In}_{0.2}\text{Ga}_{0.8}\text{As}/\text{GaAs}$  MQW is shown in Fig. 3-6.<sup>32</sup> The actual excitonic lines appear broadened due to fluctuations of the well widths during the growth process. However, the  $n = 1$  excitonic peak is clearly resolvable even at room temperature. In most bulk material systems, the exciton is only observable at low temperatures.

In the  $\text{InGaAs}/\text{GaAs}$  material, the well supports two bound states resulting in a two step absorption spectrum. However, there are two observed excitonic peaks for the first bound state attributed to transitions from the heavy and light hole states in the valence band to the first energy level of the conduction band. In bulk systems, the heavy and light hole bands are degenerate at  $k = 0$ . This results in only one excitonic peak. In 2-d structures, the bands are no longer degenerate at  $k = 0$  resulting in two possible transitions at the  $n = 1$  state. This splitting between the light and heavy hole states increases as the well width decreases.

This section has discussed optical absorption in quasi 2-d quantum well structures without the presence of an applied electric field. The next section discusses how the presence of an electric field changes the absorption coefficient. The ability to change the absorption coefficient is required to balance

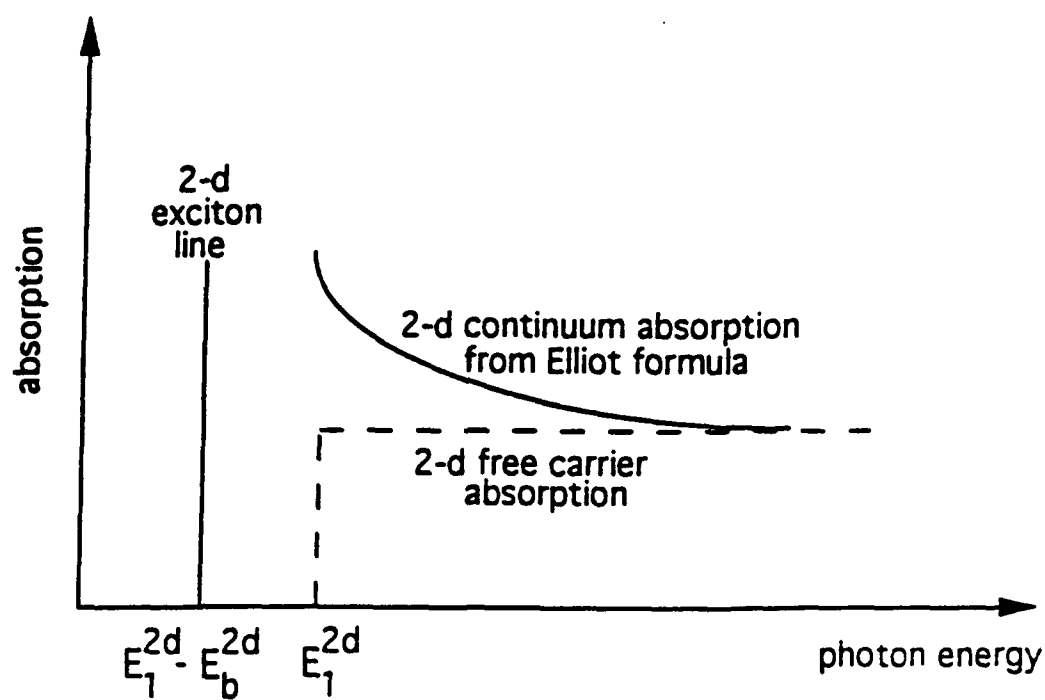


Figure 3-5 Schematic comparison of the 2-d free carrier (dashed line) and excitonic (solid line) optical absorption spectra

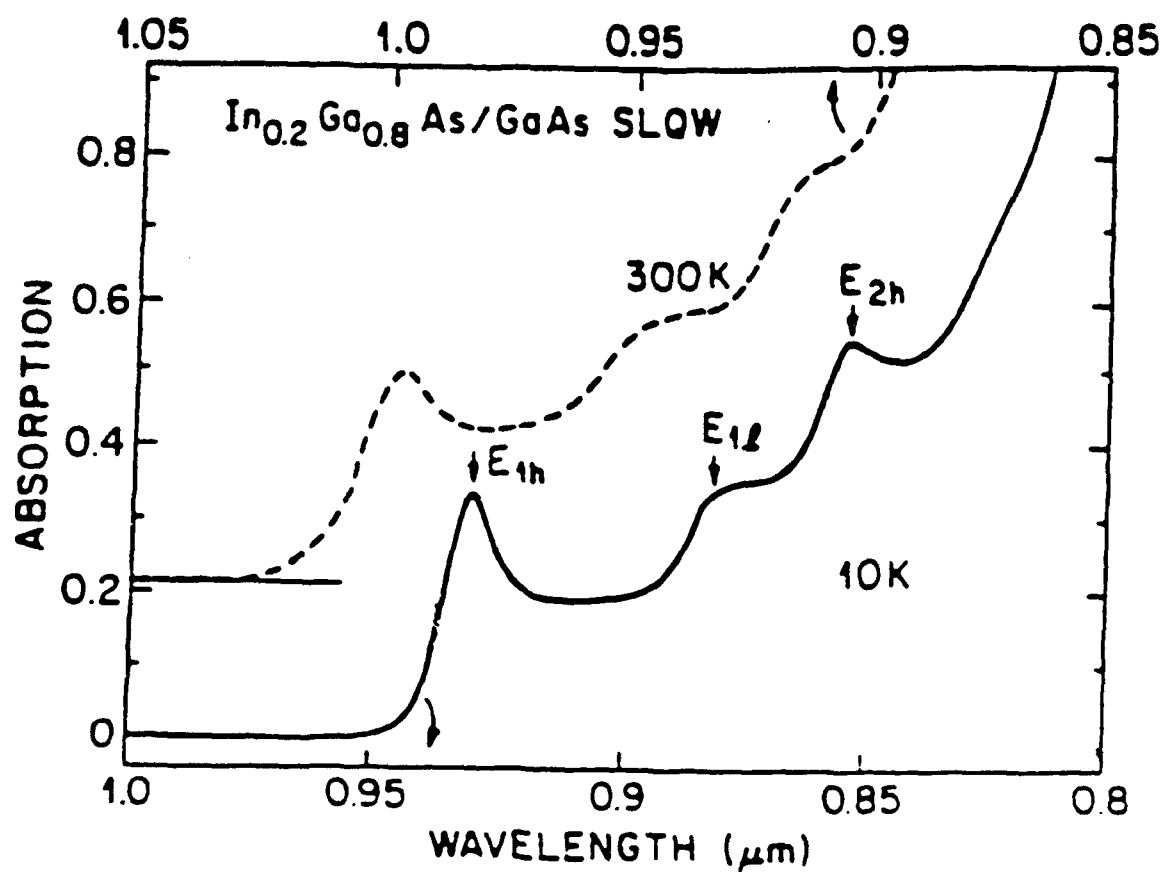


Figure 3-6 Optical absorption spectrum of an  $\text{In}_{0.2}\text{Ga}_{0.8}\text{As}/\text{GaAs}$  MQW sample (after ref. 32)

the cavity of the ARM, thus making it possible to achieve a large contrast ratio.

### 3.3 Electro-Optical Properties of Quantum Wells

The absorption coefficient of semiconductor materials is modified when an external electric field is applied. The electro-absorption in quasi 2-d structures differs considerably from the electro-absorption in bulk 3-d materials. The electro-absorption in bulk materials will first be briefly summarized before the effects of an applied electric field on quantum well structures are discussed.

The effects of an electric field on a bulk semiconductor were first described separately in 1958 by Franz and Keldysh.<sup>33</sup> This simple model is known as the Franz-Keldysh (FK) effect and neglects coulombic interaction between an electron and a hole pair. In the FK effect, the applied field causes the absorption spectra to broaden and shift to lower energies or longer wavelengths. This red shift of the band edge results in non-zero absorption below the bandgap. In addition to the red shift, the absorption spectrum develops ripples for energies above the band edge of the material.

The FK effect is a time dependent process and the red shift of the bandedge is the result of photon assisted tunneling between the conduction and valence band. A photon that has energy less than  $E_g$  can move an electron from the valence band to the conduction band if the electric field makes up for the energy deficiency. This

effect is shown in Fig. 3-7. Thus, an electron will be promoted to the conduction band if  $E_g = \hbar\omega + qE_0\Delta z$ , where  $q$  is the electron charge,  $E_0$  is the applied electric field and  $\Delta z$  is the tilt of the conduction band due to the applied field.

The Franz-Keldysh effect is enhanced when coulombic effects are included in the model. The applied field causes the excitonic resonances to broaden considerably and also shift to lower energies. This shift is known as the dc-Stark effect. The applied field now makes it easier for the electron and hole pair to separate, or ionize. The field ionization results in the broadening of the exciton resonance. The amount of red shift of the excitons is quadratically proportional to the strength of the field. However, this shift is usually small because the exciton is destroyed by the electric field before there is significant Stark shift.

In quasi 2-d quantum well structures, the electric field can be applied either parallel or perpendicular to the layers. The electro-absorption of the quantum wells resembles that of bulk 3-d materials when the field is applied parallel to the layers. Only the motion of the carriers in the x-y plane are affected by the field. Since these particles are free to move in a continuum, the electro-absorption will be similar to that in bulk materials. The main effect of electric fields applied parallel to the MQW layers is a broadening of the exciton resonances and a non-zero absorption coefficient below the bandedge. Fig. 3-8 shows the electro-absorption spectra for different field strengths applied

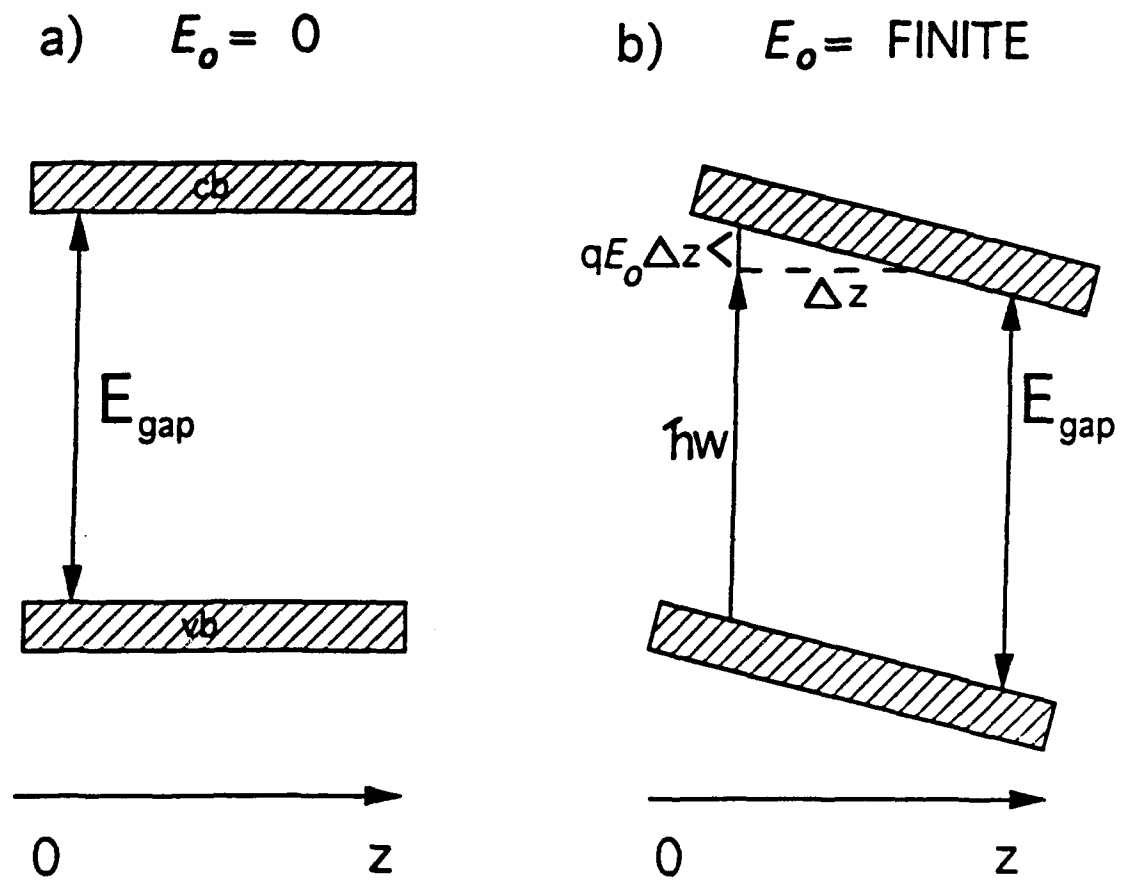


Figure 3-7 Effect of applying an electric field on the energy states in a semiconductor for a)  $E_o=0$  and b)  $E_o=\text{finite}$

parallel to a MQW structure.<sup>34</sup>

The effects of electric fields applied perpendicular to the MQW layers is very different from bulk or quasi 2-d parallel electro-absorption. Fig. 3-9 shows the absorption spectra of an MQW structure with applied perpendicular fields as a function of electron energy. The absorption edge now shifts to lower energies, but remains quite sharp. The distinguishing feature of perpendicular fields is that the exciton resonances shift to lower energies, but remain well resolved even at very high fields of approximately one hundred times the classical ionization field.<sup>35</sup>

The description of these effects will be broken up into two parts. First, the coulombic effects are neglected and the electro-absorption is modelled as the quantum confined Franz-Keldysh effect (QCFK). The coulombic effects are very important however and they are fully described by the quantum confined Stark effect (QCSE) model.

The QCFK effect is best understood by first looking at the case of a QW with infinitely deep barrier potentials. All the energy states are bound by the well and the wavefunctions are zero at both sides of the well. Both the conduction and valence bands tilt when an electric field is applied perpendicular to the QW. Fig. 3-10 shows the bands and wavefunctions in the presence of an electric field.

The electric field pushes the electron and hole wavefunctions to opposite sides of the well because of the opposite charges of the particles. The overlap between the corresponding wavefunctions

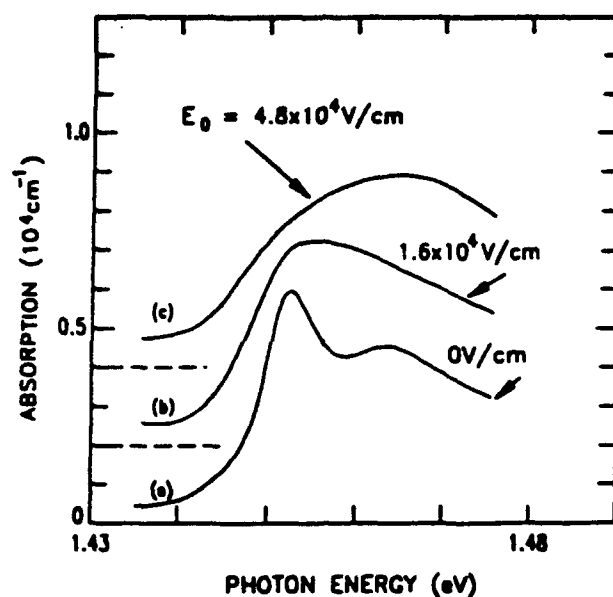


Figure 3-8 Electro-absorption for electric fields applied parallel to the plane of the layers in MQW sample, a) 0 V/cm, b)  $1.6 \times 10^4$  V/cm, c)  $4.8 \times 10^4$  V/cm (after ref. 34)

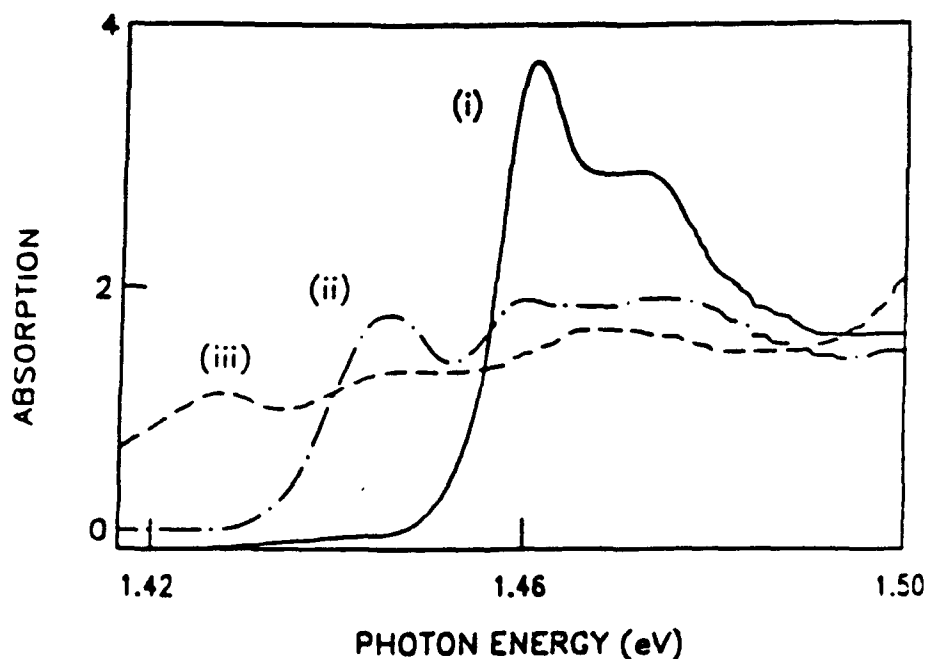


Figure 3-9 Electro-absorption for electric fields applied perpendicular to the plane of the layers in MQW sample, i)  $1.6 \times 10^4$  V/cm, ii)  $1.3 \times 10^5$  V/cm, iii)  $1.8 \times 10^5$  V/cm (after ref. 35)

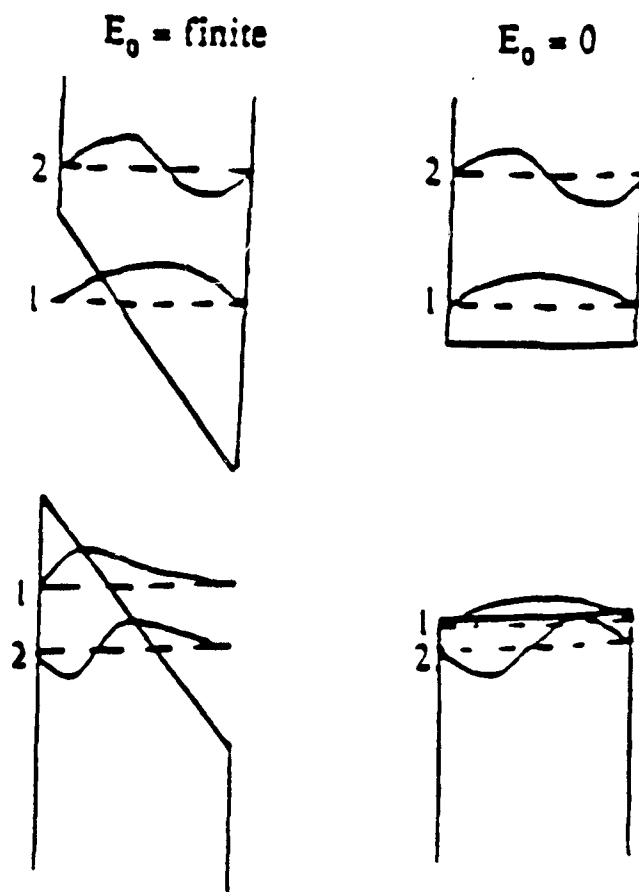


Figure 3-10 The effect of an applied electric field on the energy bands and wavefunctions in a quantum well

for the electrons and holes is now modified. The  $m = n = 1$  transition, which is the lowest allowed transition in unbiased quasi 2-d structures, is now less likely to occur because the wavefunctions have less overlap. This results in reduced absorption for the first bound state transitions.

The strict transition rules for unbiased quasi 2-d structures are no longer valid when the field is applied perpendicular to the quantum wells. In the unbiased state, transitions only occur when  $m = n$ . When a field is applied, the higher hole levels start to acquire finite overlap with the first and second electron levels. This results in new allowed transitions from:  $n = 2$  to  $m = 1$ ,  $n = 3$  to  $m = 1$ , and  $n = 1$  to  $m = 2$ . It is important to note that each hole level has a heavy and light hole subband associated with it. Fig. 3-11 shows photocurrent spectra of a AlGaAs/GaAs MQW structure with perpendicular fields of different magnitudes applied across it.<sup>36</sup> The new allowed transitions are clearly observable and become stronger as the field magnitude increases.

The QCCK effect explains why the absorption is reduced for the first heavy and light hole transitions and why excitons appear for previously unallowable transitions. However, the QCSE must be used to explain why the exciton resonances remain sharp even for very high fields. As discussed earlier, the electric field pushes the electrons and holes to opposite sides of the well. The excitonic field ionization is now restricted because of the confinement of the holes and electrons. Even for very large fields, the electron and hole pair cannot be destroyed because of this confinement and

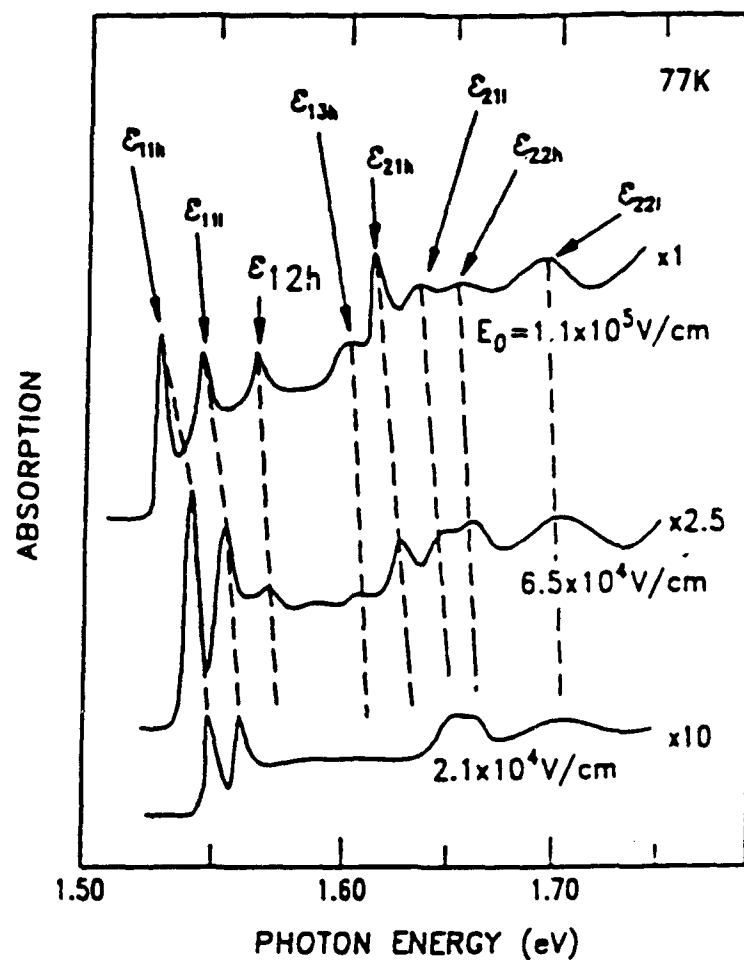


Figure 3-11 Photocurrent spectrum for a MQW at three different applied electric fields. The photocurrent spectrum effectively gives the absorption spectrum of the MQW (after ref. 36)

the excitonic peaks remain well resolved.

In addition to remaining very distinct, the exciton resonances also shift to lower energies. This shift can be rather large since it is quadratically proportional to the magnitude of the applied field. In the parallel applied field case, exciton broadening dominated the absorption spectra and there was very little dc Stark shift. This red shift is now larger because the exciton cannot be effectively destroyed by the field and can shift to lower energies. The red shift is therefore greatly enhanced by the confinement factor of the wells. This effect is appropriately named the quantum confined Stark effect.

The QC FK and QCSE are used extensively in the design and operation of the ARM. The absorption edge of the MQW region is positioned so that there is very little absorption at the operating wavelength of the etalon. The etalon is consequently designed to be unbalanced at zero field and therefore has a high reflectance. The application of a perpendicular electric field shifts the absorption edge of the MQW region to longer wavelengths thereby increasing the absorption of the cavity. The etalon is now balanced and the initially reflected light is effectively canceled out by destructive interference resulting in a near zero reflectance. High contrast ratio modulation can be achieved in this manner.

This section has discussed the use of the quantum confined Franz-Keldysh and Stark effects to shift the absorption edge of the MQW region to longer wavelengths as a perpendicular electric

field is applied. These quantum effects will be observed in the next chapter for InGaAs/GaAs MQWs and then exploited in Chapter 5 to design the ARM so that a large contrast ratio and low insertion loss can be achieved.

## Chapter 4

### Electro-absorption Characterization of InGaAs/GaAs Multiple Quantum Wells

This chapter discusses the growth, processing and characterization of InGaAs/GaAs multiple quantum wells (MQWs) used for the spacer region of the ARM. Transmission measurements were used to characterize the electro-absorption of the multiple quantum wells. The absorbance of the MQW material is derived from the transmission measurements and is a needed value in the design of the ARM.

#### 4.1 Growth and processing of InGaAs/GaAs quantum wells

A 35 period 80 Å  $\text{In}_{0.16}\text{Ga}_{0.84}\text{As}$ / 80 Å GaAs multiple quantum well system was fabricated by molecular beam epitaxy (MBE).<sup>30</sup> A biased structure is required for the purpose of characterizing the electro-absorption, i.e. the quantum confined Franz-Keldysh and Stark effects, of the quantum wells. For this reason, the MQWs were grown as the intrinsic region in a p-i-n diode on a  $n^+$  GaAs substrate. The p-i-n diode structure is shown in Fig. 4-1. The following components were stacked in order following the  $n^+$  GaAs substrate: 1) 0.4  $\mu\text{m}$  GaAs, Si doped with a concentration of  $2 \times 10^{18} \text{ cm}^{-3}$ , 2) 35 periods of 80 Å  $\text{In}_{0.16}\text{Ga}_{0.84}\text{As}$ / 80 Å GaAs MQWs, 3) 0.2  $\mu\text{m}$  GaAs, undoped, 4) 0.2  $\mu\text{m}$  GaAs, Be doped with a concentration of

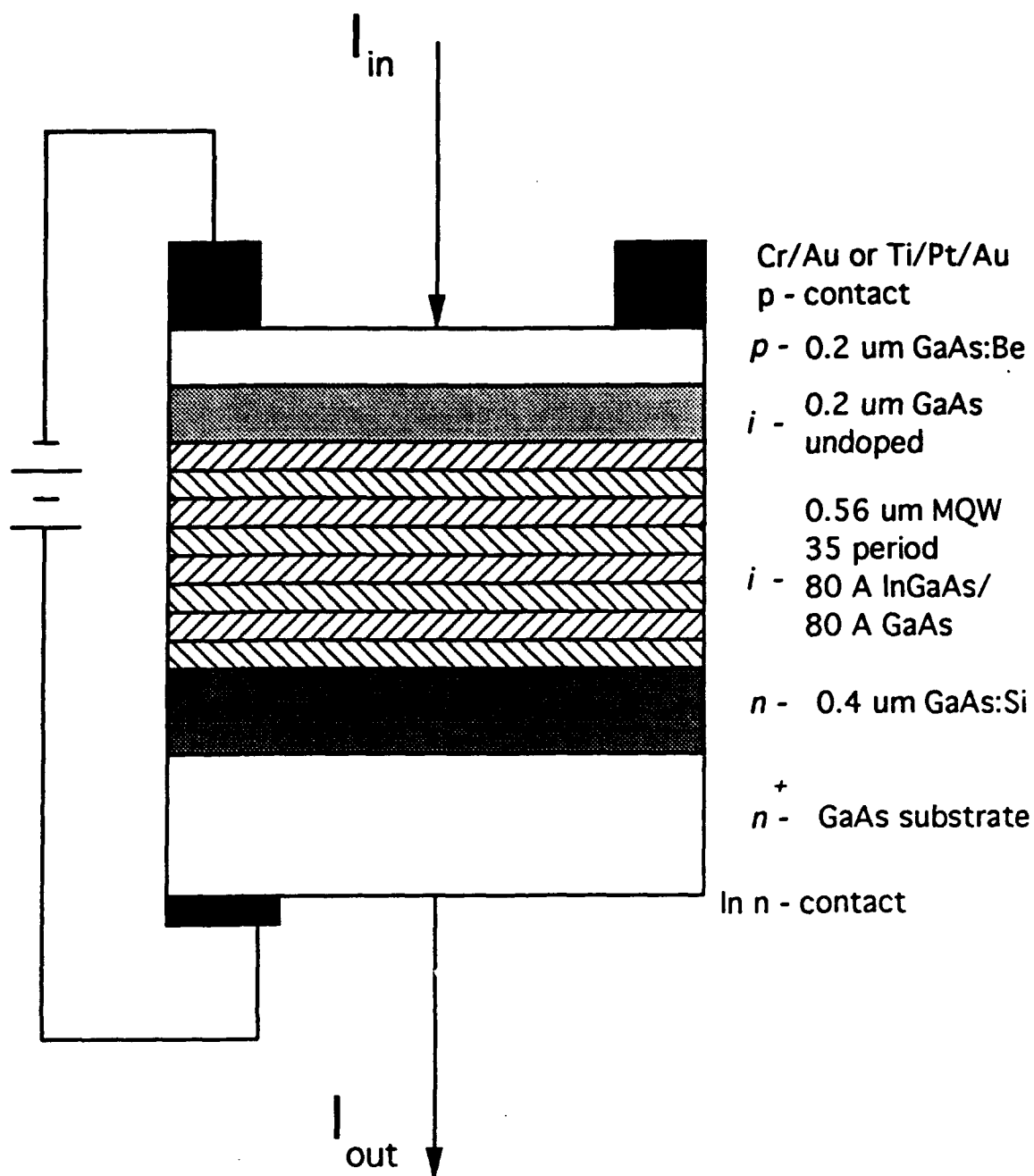


Fig. 4-1 Cross section of p-i-n diode structure

$1 \times 10^{19} \text{ cm}^{-3}$ . The room temperature photoluminescence spectrum of this structure is shown in Fig. 4-2. This spectrum shows a luminescence peak located at approximately 945 nm, corresponding to the first allowed transition associated with the heavy hole exciton.

Two different diode structures were fabricated for this work. The first diode structure uses an annular ring p-contact with a large bond pad connected to it. The active optical area is inside the annulus. Three different sizes of this device were fabricated. The largest device is fabricated as a  $1060 \mu\text{m} \times 2070 \mu\text{m}$  mesa on which the annular contact and bond pad is placed. The optical window is  $500 \mu\text{m}$  in diameter. The two other annular contacts were fabricated on  $660 \mu\text{m} \times 1570 \mu\text{m}$  and  $660 \mu\text{m} \times 1270 \mu\text{m}$  mesas. The optical windows are  $250 \mu\text{m}$  and  $100 \mu\text{m}$ , respectively.

The second diode structure consists of a square mesa with a smaller square p-contact in one corner of the mesa plateau. Four different sizes of this device were fabricated. The mesa sizes are:  $200\mu\text{m} \times 200\mu\text{m}$ ,  $400\mu\text{m} \times 400\mu\text{m}$ ,  $600\mu\text{m} \times 600\mu\text{m}$ , and  $800\mu\text{m} \times 800\mu\text{m}$ . The p-type contact is sized proportionally to the size of the mesa. The optical area is anywhere on the mesa outside of the contact. An illustration of the photolithographic mask used in the fabrication is found in Appendix A.

The annular contacts, as compared to the square contacts, should provide a more uniform electric field distribution across the optically active device area. However, the modulation speed of the ARM is R-C time constant limited. The 3 dB cutoff frequency

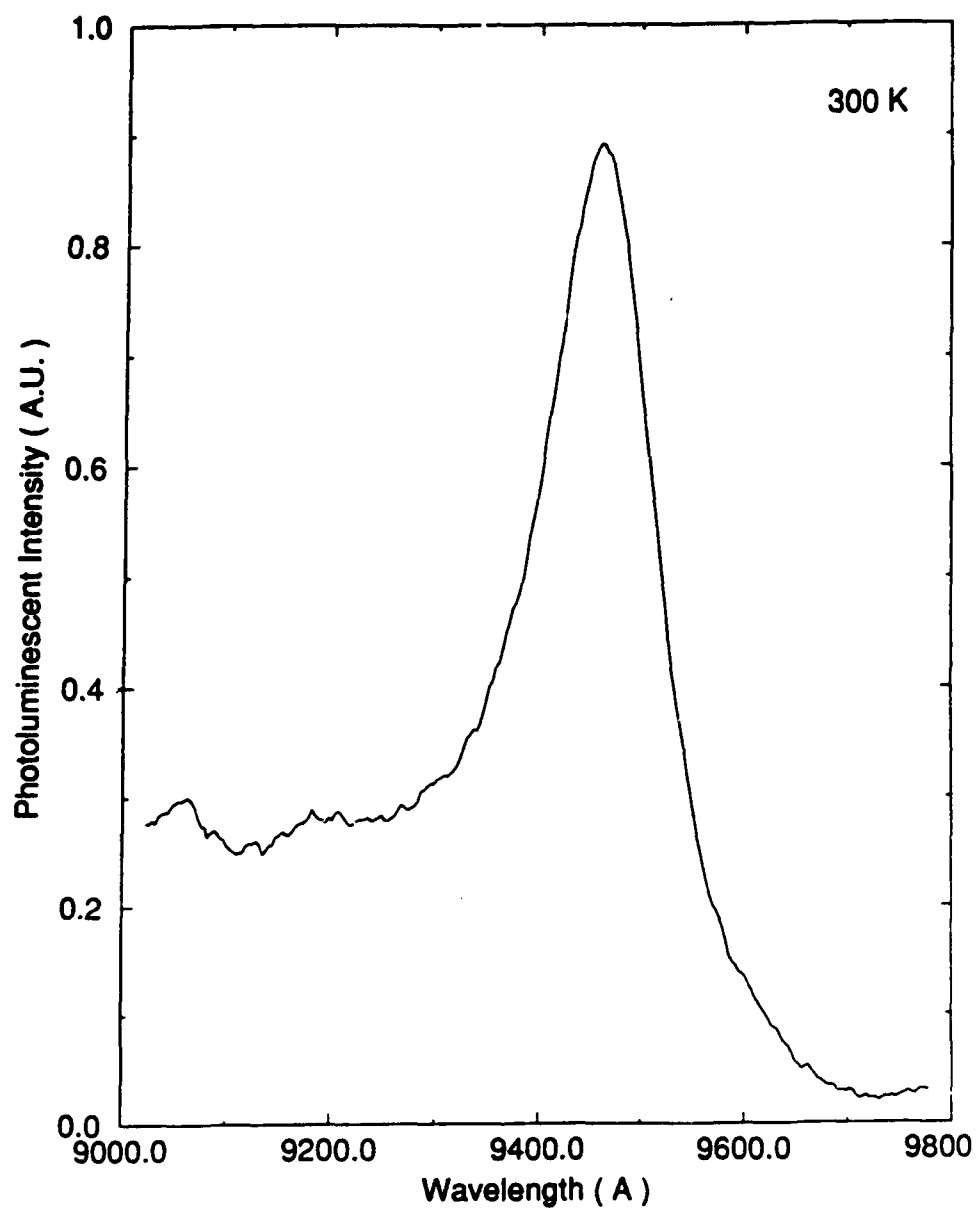


Fig. 4-2 Room temperature photoluminescence spectrum of 80 Å  $\text{In}_{0.16}\text{Ga}_{0.84}\text{As}/80 \text{ \AA GaAs MQWs}$

for the device is given by<sup>37</sup>

$$v = \frac{1}{2\pi RC_{\text{mod}}} \quad (4.1)$$

where  $R$  is the series resistance of the external circuit and  $C_{\text{mod}}$  is the capacitance of the modulator. The 3 dB cutoff frequency is the speed limitation of the device dependent upon the time required to charge the capacitor,  $C_{\text{mod}}$ , through the source resistance,  $R$ , which is assumed to be 50 ohms. Therefore, the speed of the device can be increased by reducing the capacitance.  $C_{\text{mod}}$  is given by

$$C_{\text{mod}} = \frac{\epsilon A}{d} \quad (4.2)$$

where  $\epsilon$  is the permittivity of the MQWs,  $A$  is the surface area of the mesa, and  $d$  is the total thickness of the MQW region. The capacitance of the device is decreased by reducing the surface area of the diode. Thus, the smallest square mesa should be capable of providing the fastest electrical response.

The diode processing steps are fully described in Appendix A, but a brief summary of the steps follows. The first step in fabricating the diodes was to define the mesas. This was done using photolithography and a 10:1 citric acid:H<sub>2</sub>O<sub>2</sub> wet chemical etch. The material was etched into the n-GaAs region of the diode so that electrical isolation was provided between all of the mesas on the wafer. The p-contacts were formed in the second processing

step using a standard liftoff technique. The p-contact consisted of 200 Å of chromium followed by 1500 Å of gold. This contact did not need to be annealed to form an ohmic contact. The substrate of the wafer was then mechanically polished to both thin the sample and provide a smooth surface, thus reducing the absorption associated with the substrate and the scattering loss of the substrate. Finally, a small piece of indium solder was placed in one corner of the substrate and melted on a hot plate at approximately 200°C to provide a broad n-type contact on the backside of the wafer.

#### 4.2 Electro-absorption experimental setup and results

The transmission spectra of the InGaAs/GaAs multiple quantum wells were measured using the experimental setup shown in Fig. 4-3. The luminescence from a continuous-wave argon pumped Ti:Sapphire crystal was used as the broadband optical source. The luminescence of the crystal covered the spectral range of interest, i.e. 900 nm through 1000 nm. A Schott RG-665 filter was used to block any unabsorbed or scattered light from the argon laser. The intensity of the Ti:Sapphire luminescence was controlled with a variable neutral density filter.

The broadband and collimated luminescence is focused onto the sample at normal incidence with a 5 cm plano-convex lens. The resulting spot size is approximately 50 microns in diameter. This diameter is small enough to fit on any of the diodes without

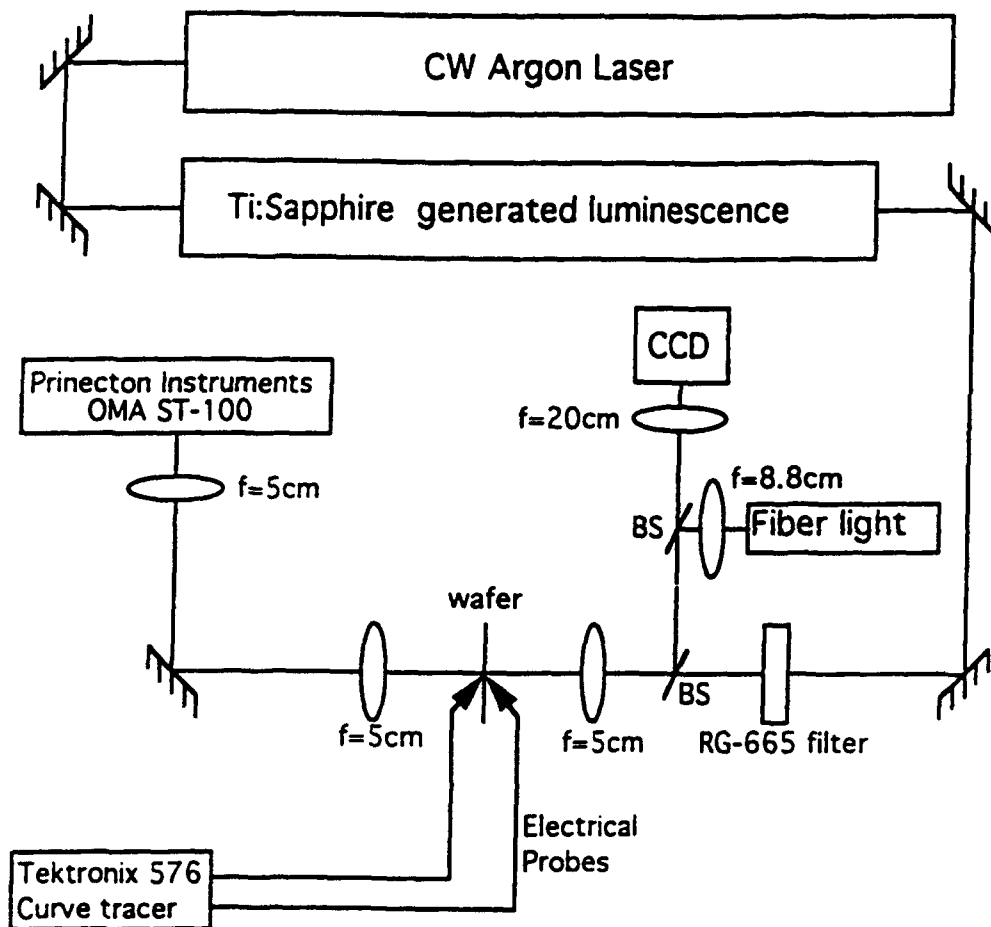


Fig. 4-3 Schematic diagram of transmission experiment  
( $f$ =focal length, BS=beamsplitter)

overfilling the mesa. An imaging system using a CCD camera, two beamsplitters, and two objectives was constructed to facilitate positioning the sample as well as the electrical probe on the contacts. The sample is mounted on a 3-d micropositioner and moved relative to the incident spot.

The light transmitted through the sample is collected and collimated with a plano-convex lens and then focused onto a calibrated detector. The detector is a calibrated spectrometer/diode array (Princeton Instruments Model ST-100) used in conjunction with an optical multichannel analyzer (OMA). The transmission as a function of wavelength is recorded by the OMA. All transmission experiments were performed at room temperature.

The reverse bias voltage was applied to the diode using a Tektronix Model 576 curve tracer. The curve tracer also allowed the I-V characteristics of the diodes to be observed to ensure good ohmic contacts had been fabricated as well as to determine the reverse breakdown fields of the diodes. The breakdown voltages varied from diode to diode, with no apparent pattern.

The transmission measurements were performed using the following calibration procedure. First, a background measurement without any Ti:Sapphire luminescence was performed to record any scattered light that was incident on the detector. Next, the transmission of the luminescence through the microscope slide on which the sample was mounted was recorded as the baseline. Finally, the transmission through the diode was recorded. The absorbance,  $\alpha L$  of the quantum wells is found from Beer's law and is

given by

$$\alpha L = -\ln\left(\frac{I}{I_0}\right), \quad (4.3)$$

where  $I$  is the transmission through the sample and  $I_0$  is the baseline transmission through the glass alone. The absorption coefficient,  $\alpha$ , is determined by dividing the absorbance,  $\alpha L$ , by the thickness of the MQW region of the diode.

The electro-absorption spectra, absorbance versus wavelength, as a function of applied electric field is shown in Fig. 4-4. The heavy hole exciton resonance at zero applied field is located at approximately 938 nm. A Stokes shift of approximately 7 nm is seen between the absorbance spectrum at zero field and the photoluminescence spectrum of Fig. 4-2.

The absorption coefficient,  $\alpha$ , as a function of applied electric field is plotted versus wavelength in Fig. 4-5. The absorption coefficient was found by dividing the absorbance values found in Fig. 4-4 by  $0.56 \mu\text{m}$  which is the total thickness of the MQW region.

The data shown in Figs. 4-4 and 4-5 were taken on an annular device that was situated on a  $660 \mu\text{m} \times 1570 \mu\text{m}$  mesa. This diode had the largest reverse breakdown voltage magnitude of any of the devices on the wafer which was -6 volts. Quantum confined Franz-Keldysh and Stark effect shifts could be observed out to -5 volts or  $6.6 \times 10^4 \text{ V/cm}$ .

The MQW region is contained almost entirely within the

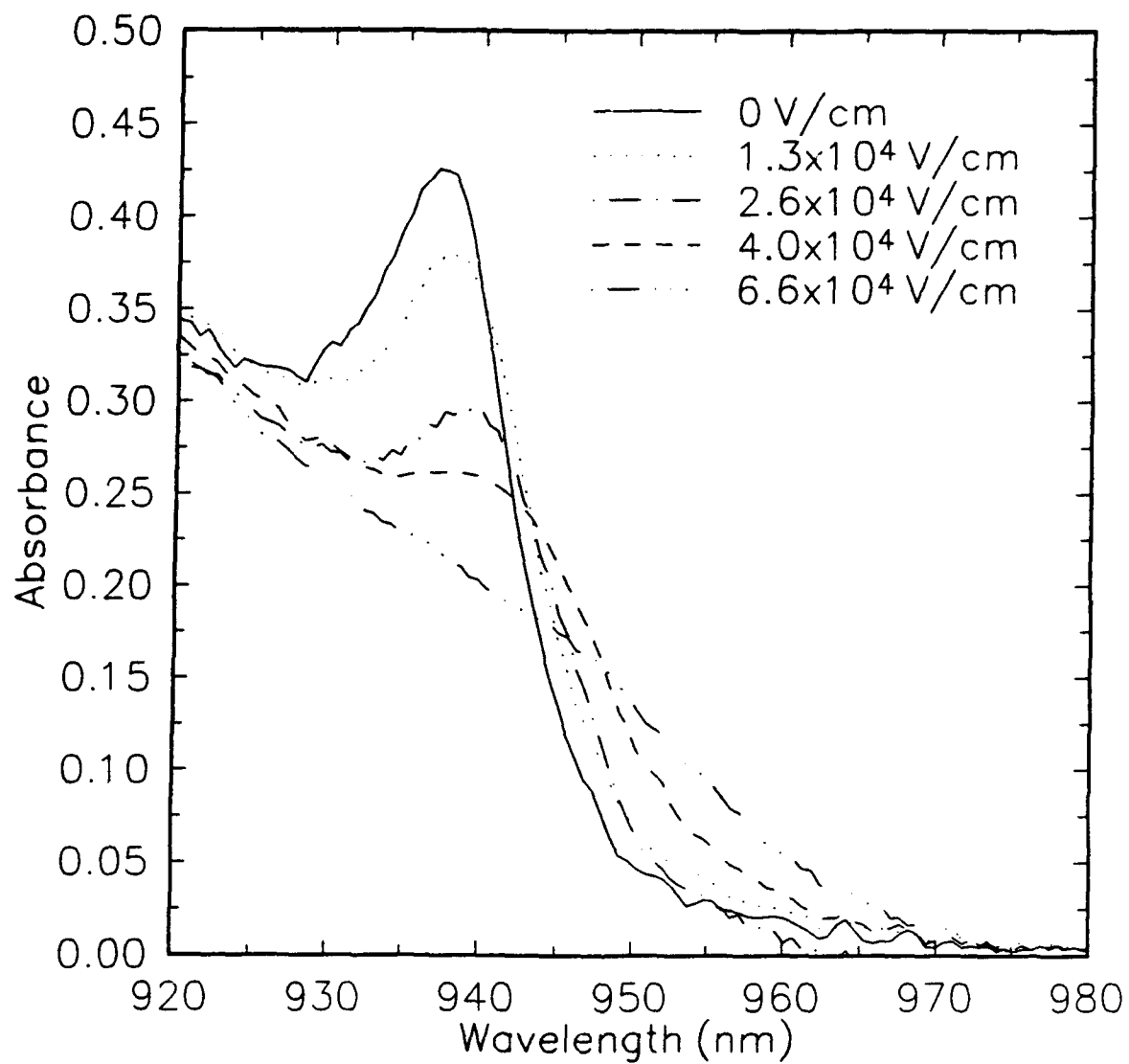


Fig. 4-4 Absorbance spectra as a function of applied electric field

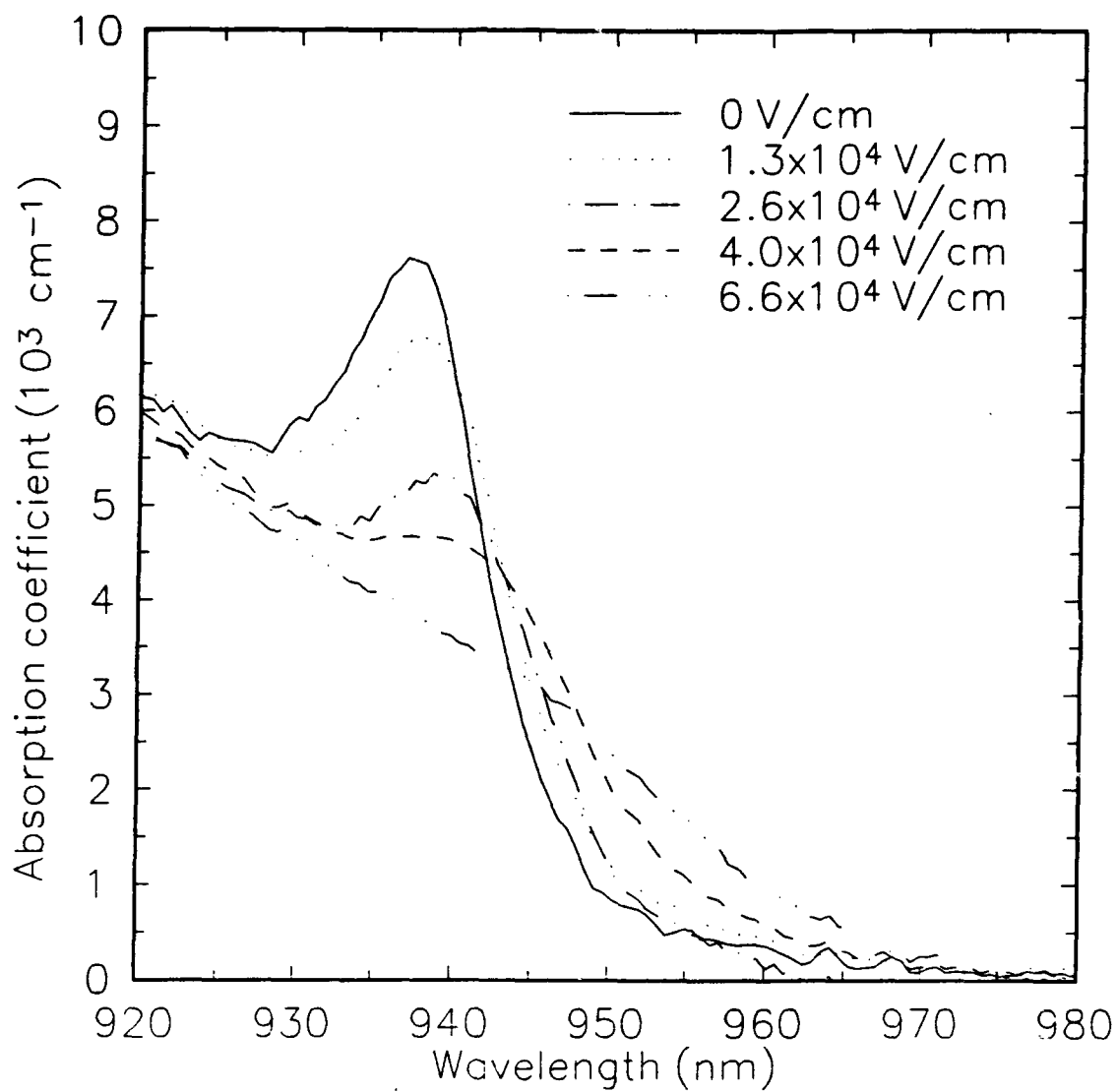


Figure 4-5 Absorption coefficient as a function of applied electric field

intrinsic region of the diode. Therefore, it is a good approximation that the electric field is equal to the applied voltage divided by the total thickness of the intrinsic region. Table 4-1 shows the electric field in the MQW region as a function of voltage that was applied across the diode.

Table 4-1 Electric field as a function of applied voltage

Applied reverse voltage (V)	Electric Field (V/cm)
-1	$1.3 \times 10^4$
-2	$2.6 \times 10^4$
-3	$4.0 \times 10^4$
-5	$6.6 \times 10^4$

The absorption spectra are seen to clearly decrease in magnitude and shift to longer wavelengths as the magnitude of the electric field is increased. The decrease in oscillator strength is seen with as little as  $1.3 \times 10^4$  V/cm applied across the diode. At  $6.6 \times 10^4$  V/cm, the exciton absorption is almost entirely bleached. These spectra are consistent with the quantum confined Franz-Keldysh and Stark effect theory discussed in Sec. 3.3.

The calculated change in absorption coefficient induced by the different electric field magnitudes, i.e. the absorption coefficient at the various applied fields minus the absorption coefficient at zero field, is plotted in Fig. 4-6. The four curves correspond to the four different applied electric fields. Fig. 4-6 shows that the largest change in the absorption coefficient occurs

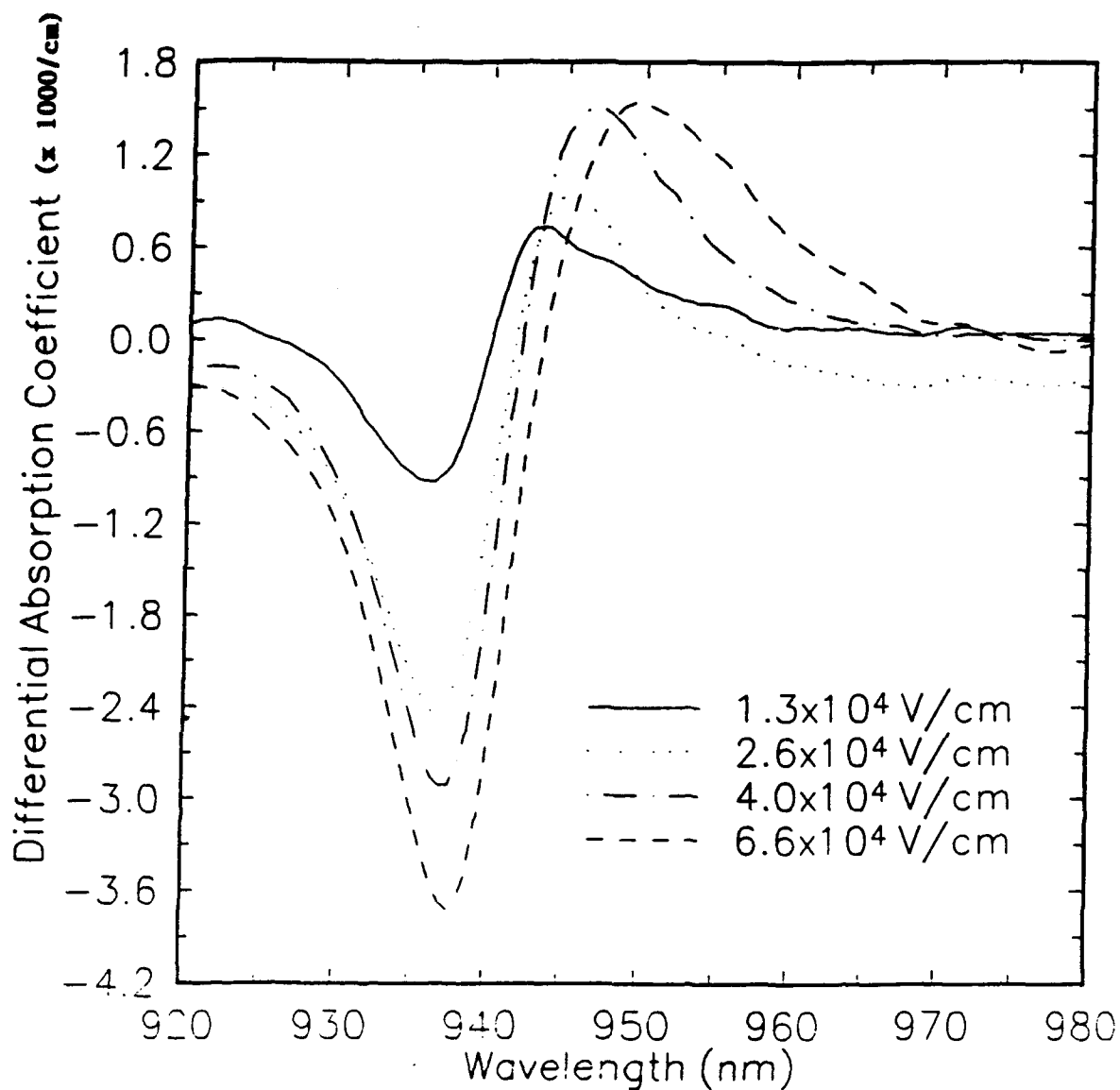


Figure 4-6 The calculated change in absorption coefficient induced by four different electric field magnitudes

at approximately 938 nm. For a -5 volt bias, or  $6.6 \times 10^4$  V/cm, the absorption coefficient changes by  $3.7 \times 10^3$  cm<sup>-1</sup>. Therefore, the ARM should be designed at 938 nm to achieve the largest contrast ratio. This would be a "normally off" modulator as described in Chapter 1. The Stark shifts associated with these small applied voltages (greater than -5 volts) shows that a reflection modulator fabricated using these quantum wells is indeed practical and compatible with digital circuitry.

This chapter has presented electro-absorption data for a 35 period 80 Å In<sub>0.16</sub>Ga<sub>0.84</sub>As/ 80 Å GaAs MQW system. The structure was fabricated as a p-i-n diode structure so that the electric field could be nearly entirely contained within the MQW region. The data shows that it is indeed possible and practical to fabricate an asymmetric reflection modulator using this type of quantum well system as the active region. The following chapter will conclude this report with a brief explanation of how the electro-absorption effect could be used in conjunction with the asymmetric Fabry-Perot etalon of Chapter 2 to effectively design an ARM.

## Chapter 5

### Conclusions and Recommendations for Future Work

This report concludes with a brief overview of the design of an asymmetric reflection modulator (ARM). The design of the ARM incorporates the electro-absorption data from Chapter 4 along with the etalon theory from Chapter 2. A single layer technique is used to determine the number of MQW periods required and also the thickness of the p region. Finally, recommendations for future work in the design, fabrication, and growth of the ARM are presented.

#### 5.1 Design of the asymmetric reflection modulator

The electro-absorption data of Sec. 4.2 showed that the largest induced change in the absorption coefficient for the InGaAs/GaAs MQW region as a function of applied electric field was approximately  $-3.7 \times 10^3 \text{ cm}^{-1}$ . At a wavelength of 938 nm, corresponding to the heavy hole exciton peak, the electric field was  $6.6 \times 10^4 \text{ V/cm}$ . Therefore, the ARM should be designed to exploit the large absorption change at 938 nm and operate as a "normally off" modulator.

The etalon cavity length at resonance was derived in Chapter 2 and is given by Eq. (2.18) as

$$L = \frac{m\lambda_o}{2n_o}, \quad (5.1)$$

where  $m$  is the finesse order number of the etalon,  $\lambda_o$  is the operating wavelength of the device, and  $n_o$  is the index of refraction of the spacer region. The absorbance required to balance the etalon is found from Eq. (2.20) and is given by

$$\alpha L = -0.5 \ln \left( \frac{R_1}{R_2} \right), \quad (5.2)$$

where  $R_1$  and  $R_2$  are the front and back mirror reflectances of the etalon, respectively.  $R_1$  is the GaAs-air interface and is approximately equal to 0.3.  $R_2$  is the DBR reflectance at the operating wavelength and as shown in Fig. 2-4 is approximately equal to 0.95. Using these values for  $R_1$  and  $R_2$ ,  $\alpha L$  in Eq. (5.2) must equal 0.576. The absorption coefficient as determined in Sec. 4.2 at the heavy hole exciton peak is  $7.5 \times 10^3 \text{ cm}^{-1}$ . The minimum possible cavity length,  $L$ , needed to make the reflectance go to zero is then 7680 Å.

However, from Eq. (5.1) the closest allowed value for the cavity length greater than 7680 Å is 8375 Å. The value for  $n_o = 3.36$  is found from an average of the bulk refractive indices for  $\text{In}_{0.16}\text{Ga}_{0.84}\text{As}^{38}$  and  $\text{GaAs}^{28}$  that make up the cavity.  $\lambda_o$  is 938 nm, which corresponds to the heavy hole exciton peak wavelength.

Therefore, a preliminary design for the spacer region is 49 periods of 80 Å  $\text{In}_{0.16}\text{Ga}_{0.84}\text{As}$ / 80 Å GaAs. The total thickness of the MQW region is 7840 Å. A 535 Å p-GaAs cap layer is used to complete the required cavity thickness of 8375 Å.

The estimated cavity length should result in a near zero reflectance at zero applied field. As the electric field is increased to  $6.6 \times 10^4$  V/cm, the cavity will become unbalanced due to the nonlinear electro-absorption of the MQWs, resulting in a non-zero reflectance. Since a large change in the absorption coefficient was observed in the electro-absorption measurements in Sec. 4.2, a large contrast ratio is expected.

## 5.2 Conclusions and recommendations for future work

This thesis has reported the fabrication and electro-absorption characterization of p-i-n diode structures containing  $\text{In}_{0.16}\text{Ga}_{0.84}\text{As}$ /GaAs multiple quantum wells as the intrinsic region. Changes in the absorption coefficient as large as  $-3.7 \times 10^3 \text{ cm}^{-1}$  were observed for an applied electric field of  $6.6 \times 10^4$  V/cm. This large change in the absorption coefficient was then used to design the cavity of an asymmetric Fabry-Perot reflection modulator which has the potential to exhibit a large on/off contrast ratio.

A 15 period GaAs/AlAs distributed Bragg reflector was also fabricated and characterized. This reflector was found to have a very high reflectance over a 100 nm spectral range. Although this DBR was centered at 970 nm, the thickness of the layers could

easily be changed so that a reflectance of over 99% could be achieved at 938 nm which corresponds to the design wavelength of the ARM. The required thicknesses of the GaAs and AlAs layers to center the DBR at 938 nm are 66.0 nm and 79.2 nm, respectively.

The p-i-n diode structures characterized in this thesis were grown on (100) GaAs substrates. These substrates do not allow any internal strain generated electric fields to be produced. However, (110) GaAs substrates do allow internal strain generated electric fields to be produced. Therefore, the electro-absorption of InGaAs/GaAs MQWs could be enhanced if the structures were grown on (110) substrates. This may result in a higher contrast ratio and a lower insertion loss in the asymmetric reflection modulator at reduced drive voltages.

## Appendix A

### Fabrication and Processing Techniques for P-I-N Structures

The fabrication process steps of the p-i-n diode structures are outlined as follows. It is important to note that the exact same processing steps would be followed in the fabrication of an asymmetric reflection modulator.

The photolithographic mask used in the fabrication process is shown in Fig. A-1. Plates numbered 1 and 3 were used in the fabrication of the square devices, while plates 4 and 6 were used in the fabrication of the annular devices. Plates 2 and 5 were designed for an additional protective oxide on the sides of the mesas. The formation of the protective oxide was not used in the fabrication of the diodes for this work.

#### P-I-N fabrication technique:

1. Cleave the MBE grown wafer into 0.2" x 0.22" pieces. This size piece fits into the beveller used in Step 2.
2. Bevel the edges and corners of the wafer using a 45 degree beveller and sandpaper. This prevents edge-bead photoresist buildup during the photolithography steps.
3. Clean the wafer using hot TCA, acetone, and methanol, respectively. Manually agitate the wafer in each beaker for one minute. Rinse the wafer in DI water and blow dry with N<sub>2</sub>. This

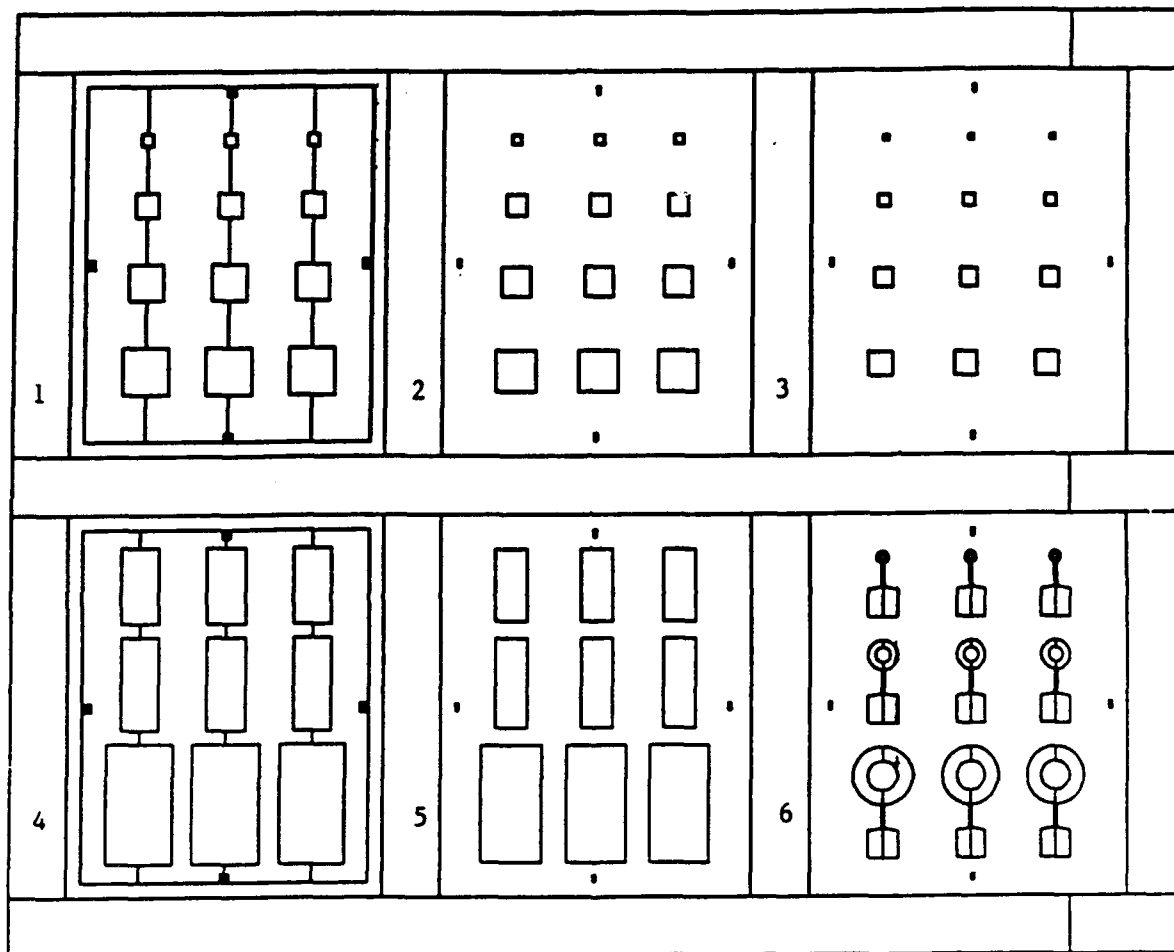


**Fig. A-1** Schematic of photolithographic mask used in the fabrication of the diodes

step should be performed twice.

4. Spin clean the wafer using TCA, ethanol, and methanol. Each solvent should be applied for approximately one minute apiece using squeeze bottles.

5. Place the wafer in the  $O_2$  plasma etcher for four minutes. This step will remove any organics on the wafer.

6. Bake-out the wafer on a hot plate at  $120^\circ C$  for 5 minutes. This step will remove any moisture in the wafer.

7. Place a few drops of HMDS photoresist adhesion promoter on the wafer and spin for 30 seconds.

8. Spin AZ4110 photoresist on the wafer at 6000 rpms for 30 seconds. Approximately  $1.1\ \mu m$  of photoresist is deposited.

9. Soft bake the wafer on a hot plate at  $100^\circ C$  for 45 seconds.

10. Using the Karl Suss 505 mask aligner, expose the wafer for 30 seconds. Plate 1 defines the mesas for the square devices and plate 4 defines the mesas for the annular devices.

11. Develop in 4:1 DI  $H_2O$ :AZ400K for 30 seconds. Rinse in DI water for 30 seconds. Blow dry with  $N_2$ .

12. Etch the wafer in a 10:1 citric acid:DI  $H_2O_2$  wet etch. The etch rate is approximately  $0.2\ \mu m/min$ . The wafer must be etched into the n region of the diode to provide electrical isolation between the mesas. The p-i-n diodes used in this thesis were etched for 9 minutes. The etch depth may be checked with a profilometer before the photoresist is removed.

13. Rinse the wafer in acetone to remove the photoresist.

Repeat as needed, until all the photoresist is removed.

14. Repeat steps 3 through 7 to thoroughly clean the wafer and re-apply the HMDS adhesion promoter.
15. Spin AZ4110 photoresist on the wafer at 8000 rpms for 30 seconds.
16. Soft bake the wafer on a hot plate at 100°C for 45 seconds.
17. Flood expose the wafer in the mask aligner for 30 seconds.
18. Spin AZ4210 resist on the wafer at 7000 rpms for 30 seconds. This resist must be spun on immediately after the flood exposure to ensure that the AZ4110 resist does not breakdown.
19. Soft bake the wafer on a hot plate at 100°C for 45 seconds.
20. Using the mask aligner, expose the wafer for 20 seconds. Plate 3 defines the p contacts for the square devices and plate 6 defines the annular contacts.
21. Develop the wafer in 4:1 DI H<sub>2</sub>O:AZ400K solution for 90 seconds. Rinse in DI water for 30 seconds. Blow dry with N<sub>2</sub>.
22. Dip the wafer in BOE (buffered oxide etchant) for 20 seconds, briefly rinse with DI water, and blow dry with N<sub>2</sub>. BOE is composed of 10:1 NH<sub>4</sub>F(40%):HF(49%).
23. Mount the wafer on a microscope slide with black wax so that the photoresist is face up. It is recommended that a few drops of TCA be used to dissolve a small piece of black wax. Then, apply the wax to the microscope slide with a toothpick. This ensures an even and thorough application of the wax. Cover the slide with a petri dish and let harden for at least three minutes.
24. Place the sample in the electron beam evaporator and evaporate 400 Å of titanium, 200 Å of platinum, and 1500 Å of gold. An

alternative p-contact is 200 Å of chromium and 1500 Å of gold.

25. Place the slide in a beaker of hot acetone until all the metals and photoresist have lifted off. This should take about 5 minutes.

26. Place the slide on a hot plate and heat until the wafer can easily be slid off the black wax.

27. Thoroughly rinse the wafer in TCA, acetone, and methanol. Repeat this step until all the black wax and residue on the wafer have been removed.

28. Anneal the wafer in an anneal station with a  $N_2/H_2$  purge for 2 minutes at 400°C. Check the p-contact with a curve tracer to ensure that an ohmic contact has been formed. The wafer should only be annealed if the Ti-Pt-Au contacting scheme was used. Cr-Au contacts should never be annealed.

29. Using a mechanical polisher and 3  $\mu m$ , 1  $\mu m$  and 0.3  $\mu m$  aluminum oxide polishing paper, respectively, polish the substrate until a dull to medium shine has appeared.

30. Form the backside contact by placing a small drop of indium solder in one corner of the backside of the wafer and heat on a hot plate at approximately 200°C. Lightly pressing on the indium ensures that it penetrates into the substrate.

## REFERENCES

1. J.W. Goodman, F.J. Leonberger, S.Y. Kung, and R.A. Athale, *Proc. IEEE* 72 850 (1984).
2. R.W. Keyes, *Proc. IEEE* 63 740 (1975).
3. R.K. Boncek, P.R. Prucnal, M.F. Krol, S.T. Johns, and J.L. Stacy, *Optical Engineering* 31 2442 (1992).
4. D.Z. Tsang, *Opt. Photon. News* 23 (October 1990).
5. S.E. Elby and P.R. Prucnal, *Proc. SPIE* 994 77 (1988).
6. P.R. Prucnal, *Proc. SPIE* 703 106 (1986).
7. H.F. Bare, F. Haas, D.A. Honey, D. Mikolas, H.G. Craighead, G. Pugh, and R. Soave, *IEEE Phot. Tech. Lett.* 5 172 (1993).
8. M.R. Feldman, *Connect. Technol.* 26 (May 1992).
9. J.L. Jewell, J.P. Harbison, A. Scherer, Y.H. Lee, and L.T. Florez, *IEEE J. Quantum Electron.* 27 1332 (1991).
10. K.F. Huang, K. Tai, S.N.G. Chu, and A.Y. Cho, *Appl. Phys. Lett.* 54 2026 (1989).
11. I.J. Fritz, B.E. Hammons, A.J. Howard, T.M. Brennan, and J.A. Olsen, *Appl. Phys. Lett.* 62 919 (1993).
12. C. Amano, S. Matsuo, T. Kurokawa, and H. Iwamura, *IEEE Phot. Tech. Lett.* 4 31 (1992).
13. C. Rolland, G. Mak, K.L. Prosyk, C.m. Maritan, and N. Puetz, *IEEE Phot. Tech. Lett.* 3 894 (1991).
14. K. Hu, L. Chen, A. Madhukar, P. Chen, K.C. Rajkumar, K. Kaviani, Z. Karim, C. Kyriakakis, and A.R. Tanguay, Jr., *Appl. Phys. Lett.* 59 1108 (1991).
15. R. Hull, J.C. Bean, F. Cerdeira, A.T. Fiory, and J.M. Gibson, *Appl. Phys. Lett.* 48 56 (1986).
16. R. People, and J.C. Bean, *Appl. Phys. Lett.* 47 322 (1985).

17. J.J. Rosenberg, M. Benlamri, P.D. Kirchner, J.M. Woodall, and G.D. Pettit, *IEEE Electron Device Lett.* EDL-6 491 (1985).
18. G.E. Bulman, D.R. Myers, T.E. Zipperian, and L.R. Dawson, *Appl. Phys. Lett.* 48 1015 (1986).
19. T.E. Van Eck, P. Chu, W.S.C. Chang, and H.H. Wieder, *Appl. Phys. Lett.* 49 135 (1986).
20. M. Whitehead, A. Rivers, G. Parry, J.S. Roberts, and C. Button, *Electron. Lett.* 25 984 (1989).
21. M. Whitehead, A. Rivers, G. Parry, and J.S. Roberts, *Electron. Lett.* 26 1588 (1990).
22. D.S. Chemla, D.A.B. Miller, and S. Schmitt-Rink, in *Optical Nonlinearities and Instabilities in Semiconductors*, edited by H. Haug (Academic Press, Inc., 1988), pp. 83-120.
23. M. Whitehead, and G. Parry, *Electron. Lett.* 25 566 (1989).
24. R.H. Yan, R.J. Simes, and L.A. Coldren, *IEEE Phot. Tech. Lett.* 1 273 (1989).
25. A. Yariv, *Optical Electronics* (Saunders College Publishing, Philadelphia, 1991).
26. J.M. Vigoureux, *J. Opt. Soc. Am. A* 8 1697 (1991).
27. M.F. Krol, Rome Laboratory Photonics Center.
28. E.D. Palik, *Handbook of Optical Constants of Solids* (Academic Press, Boston, 1985).
29. M.A. Afromowitz, *Solid State Commun.* 15 55 (1974).
30. E.T. Towe and D.C. Sun, University of Virginia Electrical Engineering Department.
31. N. Peyghambarian, S.W. Koch, A. Mysyrowicz, *Introduction to Semiconductor Optics* (Prentice Hall, Englewood Cliffs, New Jersey, 1993).
32. K.F. Huang, K. Ta S.N.G. Chu, and A. Y. Cho, *Appl. Phys. Lett.* 54 2026 (1989).
33. L.V. Keldysh, *Soviet Physics, JTEP* 7 788 (1958); W. Franz, *Z. Naturforsch* 139 484 (1958).

34. D.A.B. Miller, D.S. Chemla, T.C. Damen, A.C. Gossard, W. Wiegmann, T.H. Wood, and C.A. Burrus, *Phys. Rev. B* 32 1043 (1985).
35. J.S. Weiner, D.A.B. Miller, D.S. Chemla, T.C. Damen, C.A. Burrus, T.H. Wood, A.C. Gossard, and W. Wiegmann, *Appl. Phys. Lett.* 47 1148 (1985).
36. K. Yamanada, T. Fukunnaga, N. Tsukada, K.L.I. Kobayashi, and M.I. Shii, *Appl. Phys. Lett.* 48 840 (1986).
37. T.H. Wood, *J. Lightwave Technol.* LT-6 743 (1988).
38. S. Nojima and H. Asahi, *J. Appl. Phys.* 63 479 (1987).

***MISSION  
OF  
ROME LABORATORY***

**Mission.** The mission of Rome Laboratory is to advance the science and technologies of command, control, communications and intelligence and to transition them into systems to meet customer needs. To achieve this, Rome Lab:

- a. Conducts vigorous research, development and test programs in all applicable technologies;
- b. Transitions technology to current and future systems to improve operational capability, readiness, and supportability;
- c. Provides a full range of technical support to Air Force Materiel Command product centers and other Air Force organizations;
- d. Promotes transfer of technology to the private sector;
- e. Maintains leading edge technological expertise in the areas of surveillance, communications, command and control, intelligence, reliability science, electro-magnetic technology, photonics, signal processing, and computational science.

The thrust areas of technical competence include: Surveillance, Communications, Command and Control, Intelligence, Signal Processing, Computer Science and Technology, Electromagnetic Technology, Photonics and Reliability Sciences.